Construction and Building Materials 363 (2023) 129805

Contents lists available at ScienceDirect

Construction and Building Materials

journal homepage: www.elsevier.com/locate/conbuildmat

# Characterization of ferrochrome ash and blast furnace slag based alkali-activated paste and mortar

Tarik Omur [a], Nausad Miyan [b], Nihat Kabay [a,*], Burak Birol [c], Didem Oktay [a]

[a] Yildiz Technical University, Department of Civil Engineering, 34220 Istanbul, Turkey
[b] LBA Design and Consultancy, 34750 Istanbul, Turkey
[c] Yildiz Technical University, Department of Metallurgical and Materials Engineering, 34210 Istanbul, Turkey

ARTICLE INFO

*Keywords:*
Alkali-activation
Ferrochrome ash
Microstructure
Rheology
Physicomechanical properties

ABSTRACT

Ferrochrome ash (FCA) is an industrial waste material which when disposed causes environmental pollution and health hazard. Therefore, in this paper, FCA replaced up to 30 % of blast furnace slag (BFS) to investigate its possible utilization by producing alkali-activated material. The effect of FCA content and varying $Na_2O$ dosage on fresh, physicomechanical and microstructural properties was discussed. The addition of FCA improved the rheological properties of mixes by reducing plastic viscosity from 47.3 to 22.9 Pa.s and from 129.2 to 71.1 Pa.s and yield stress from 87.5 to 40.7 Pa and from 89.8 to 44.0 Pa for $Na_2O$ dosage of 6 and 10 %, respectively. This allowed reduction of water content, which in turn resulted in similar or superior physicomechanical properties compared to the control mixtures. The setting time was prolonged with an increase in $Na_2O$ dosage and FCA addition and was mainly governed by the initial molar ratio of $SiO_2/Al_2O_3$. The increase in FCA ratios consistently decreased semi-adiabatic peak temperature and time to reach the peak temperature. FCA addition decreased compressive strength and drying shrinkage of mortar mixes, whereas increase in $Na_2O$ dosage significantly enhanced strength. The microstructural investigations revealed that the major reaction products of paste mixes were C—S—H, C-A—S—H, and/or M—S—H gels, along with minor phases such as forsterite, natrolite, brownmillerite, and spinel. The formation of M—S—H type gels was observed with an increased replacement ratio of FCA. In addition, the polymerization of main reaction products is found to be controlled by the Ca/Si and Si/Al ratios as revealed by microstructural analysis. The findings of this research point out the viability of producing BFS and FCA-based alkali-activated material with reasonable properties and their efficient utilization which may ensure sustainability.

## 1. Introduction

The disposal of massive volumes of waste generated by various human activities, including production, construction, mining, and quarrying, is a significant modern environmental challenge [1]. While the natural resources are consumed daily, the metal industries are expanding, and their generated solid wastes are significantly increasing. The generated industrial solid wastes impose an environmental burden along with the consumption of valuable landmass [2]. The ferrochrome industry is one of the metal industries that involves the manufacturing of ferrochrome using electric arc furnaces to obtain stainless steel [3]. Global annual ferrochrome production is estimated to be approximately 6.5–9.5 million tons, growing at a compound annual growth rate of about 3 % [4]. Approximately 2.5 million tons of chromite ore is required to produce 1 million tons of ferrochrome and the process generates 1 to1.2 million tons of solid waste [5]. Ferrochrome ash (FCA) is one of the discarded solid waste materials that is generated 0.02–0.03 tons per ton of ferrochrome production in large quantities from the gas cleaning systems during ferrochrome production [6]. The generated FCA solid waste is generally disposed and a possibility to pollute water resources or degrade the environment emerges which may consequently cause health hazards [7]. Therefore, special attention and alternative methods are required to recycle or utilize FCA wastes to minimize their associated environmental issues.

Portland cement (PC) is the most extensively utilized cementitious material in civil engineering and construction applications [8,9]. However, the PC manufacturing process is responsible for approximately 5–8% of $CO_2$ emissions throughout the world [10]. In addition, the

* Corresponding author.
*E-mail address:* nkabay@yildiz.edu.tr (N. Kabay).

https://doi.org/10.1016/j.conbuildmat.2022.129805
Received 24 August 2022; Received in revised form 10 November 2022; Accepted 16 November 2022
Available online 24 November 2022
0950-0618/© 2022 Elsevier Ltd. All rights reserved.

**Table 1**
Mixture design of AAP and AAM.

| Paste mixes | | | | | Mortar mixes | | | | |
|---|---|---|---|---|---|---|---|---|---|
| Mix ID | FCA (wt%) | BFS (wt%) | $Na_2O$ (wt%) | w/p | Mix ID | FCA (wt%) | BFS (wt%) | $Na_2O$ (wt%) | w/p |
| P0-N6 | 0 | 100 | 6 | 0.30 | M0-N6 | 0 | 100 | 6 | 0.35 |
| P0-N8 | 0 | 100 | 8 | 0.30 | M0-N8 | 0 | 100 | 8 | 0.35 |
| P0-N10 | 0 | 100 | 10 | 0.30 | M0-N10 | 0 | 100 | 10 | 0.35 |
| P10-N6 | 10 | 90 | 6 | 0.30 | M10-N6 | 10 | 90 | 6 | 0.35 |
| P10-N8 | 10 | 90 | 8 | 0.30 | M10-N8 | 10 | 90 | 8 | 0.35 |
| P10-N10 | 10 | 90 | 10 | 0.30 | M10-N10 | 10 | 90 | 10 | 0.35 |
| P20-N6 | 20 | 80 | 6 | 0.30 | M20-N6 | 20 | 80 | 6 | 0.35 |
| P20-N8 | 20 | 80 | 8 | 0.30 | M20-N8 | 20 | 80 | 8 | 0.35 |
| P20-N10 | 20 | 80 | 10 | 0.30 | M20-N10 | 20 | 80 | 10 | 0.35 |
| P30-N6 | 30 | 70 | 6 | 0.30 | M30-N6 | 30 | 70 | 6 | 0.35 |
| P30-N8 | 30 | 70 | 8 | 0.30 | M30-N8 | 30 | 70 | 8 | 0.35 |
| P30-N10 | 30 | 70 | 10 | 0.30 | M30-N10 | 30 | 70 | 10 | 0.35 |
| P10-N6* | 10 | 90 | 6 | 0.27 | M10-N6* | 10 | 90 | 6 | 0.315 |
| P10-N10* | 10 | 90 | 10 | 0.27 | M10-N8* | 10 | 90 | 8 | 0.315 |
| | | | | | M10-N10* | 10 | 90 | 10 | 0.315 |

* represents the mixes produced with 10% lower w/p ratio.

processing of each ton of PC requires around 130 kg of fuel and 110 kWh of electricity, which consequently releases approximately 0.9 tons of $CO_2$ and contributes to greenhouse gas emissions [11,12]. Research on alternative binders has been conducted for several decades with the aim of minimizing energy consumption and $CO_2$ emissions.

Alkali activated materials are low-$CO_2$ alternative materials synthesized to integrate waste aluminosilicate materials originating from various industrial processes into the production cycle of low-impact and economically sustainable construction materials [13]. In addition, these materials show superior or comparable strength and durability compared to PC-based materials [14–16]. Alkali-activated binders can be activated using several alkali solutions such as sodium carbonate ($Na_2CO_3$), potassium hydroxide (KOH), sodium hydroxide (NaOH), and sodium silicate ($Na_2SiO_3$). The development of mechanical properties in alkali-activated systems is primarily owed to the formation of chained Si-O-Al-O- networks and the formation of calcium aluminate silicate hydrate (C-A—S—H) and sodium aluminate silicate hydrate (*N*-A—S—H) gels which depends on the chemical composition of binder, activator type, and concentration, curing temperature, and pH [17–21]. Alkali-activated materials can be an alternative to PC since it can be manufactured using industrial by-products or aluminosilicate materials such as ground granulated blast furnace slag (BFS) [20,22,23], basic oxygen furnace slag [24], fly ash [25,26], glass powder [27,28], silica fume [29,30] and metakaolin [31,32].

Several studies have been reported promoting the utilization and application of FCA in replacing cement and alkali activation either in mortar or concrete. FCA and lime were used as partial replacements for cement to manufacture concrete. The incorporation of 7 % lime and 10 % FCA provided the highest compressive strength and improved durability properties of manufactured concrete [7]. Acharya and Patro [11] examined the effects of FCA and lime as partial substitutes for cement to manufacture concrete. It was reported that the addition of FCA along with lime decreased the workability; however, it ameliorated compressive, flexural, and bond strength. In addition, sorptivity reduced, and endurance to acid and sulfate attack increased with the incorporation of FCA and lime in the concrete. Kumar et al. [5] investigated various properties of alkali-activated slag based mortar in which FCA partially replaced BFS in different ratios and the results showed that the compressive strength reduced with an increase in FCA ratios. The proposed methodology to produce mortars can be environmentally friendly and reduce cost compared to mortar containing only BFS, the authors further added. Mishra et al. [4] successfully synthesized geopolymer concrete incorporating BFS, FCA, and lime. The results of the study showed that concrete containing 80 % FCA, 20 % BFS, and lime (10 % by wt of BFS) achieved the highest compressive strength of about 27 MPa.

Considering the fact that FCA waste is generally disposed without efficiently utilized and causes environment problems, the present study aims to research the potential of FCA as an alternative material in the alkali activation by examining the fresh-state and physical properties such as rheology, setting time, temperature kinetics, drying shrinkage, and water absorption along with the compressive strength development of FCA and BFS based alkali-activated mortar (AAM) activated with various $Na_2O$ dosage. The X-ray diffraction (XRD) and scanning electron microscopy (SEM) analyses were also employed to investigate the microstructure and the hydration products. In addition, a series of AAM and alkali-activated paste (AAP) containing 10 % of FCA were examined with a reduced water-to-powder (w/p) ratio based on the rheological studies. The present study may address the environmental problems and health hazards related to FCA by its utilization with BFS to produce AAM.

## 2. Methodology

### 2.1. Materials, mix proportions, and specimen preparation

FCA, utilized in the present study, was obtained from the baghouse filter of the high carbon ferrochrome production furnace located in Eti Krom Inc., Elazığ, Turkey, and BFS was obtained from a local commercial supplier. The commercially available NaOH flakes of purity $\geq$ 99 % and sodium silicate (SS) solution composed of 8.4 % and 27.8 % of $Na_2O$ and $SiO_2$, respectively, were used as alkaline activators. The mixture of NaOH and SS solution had a constant silica modulus ($SiO_2$/$Na_2O$) of 1.25, and varying $Na_2O$ content (6, 8, and 10 % by mass of powder) was used to activate the precursors. It should be noted that the amount of SS solution was proportionally increased to set silica modulus as 1.25 for increasing $Na_2O$ content. The blends of FCA and BFS were used as the solid precursor material in which FCA replaced BFS by 0, 10, 20, and 30 % by mass to produce alkali-activated paste (AAP) and AAM samples. The mixture proportions of the AAP and AAM are presented in Table 1. In the mix IDs, P and M represent paste and mortar, respectively, whereas the numbers followed by P or M denote the replacement ratios of FCA. Similarly, N and the following number stand for the percentage of $Na_2O$ dosage. In addition, the total water content of the mixes was adjusted, as shown in Table 1, by reducing the amount of water present in SS solution.

The alkaline solution was prepared by mixing NaOH and SS solution thoroughly and left to cool down to laboratory temperature in a sealed condition. The mixing was commenced by pouring the alkaline solution into the mixing bowl, followed by adding the blended powder and mixing thoroughly to obtain a homogenous paste. Similarly, siliceous sand of particle size less than 2.00 mm was employed as fine aggregate

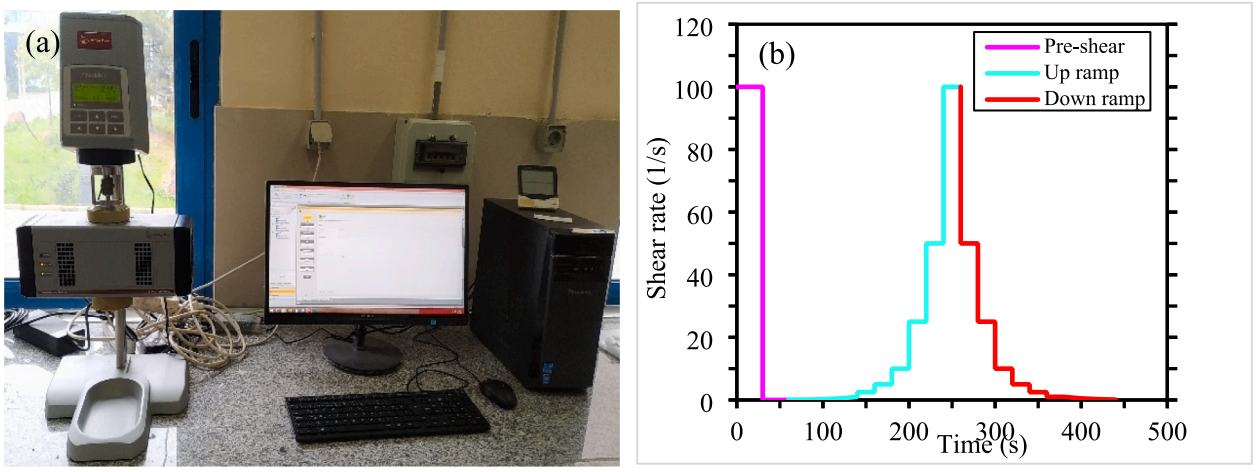



**Fig. 1.** (a) Rheology test instrument and (b) rheological testing procedure.

to manufacture mortar samples, and the powder to fine aggregate ratio was kept constant as 1:3 in each mortar production. The sand was slowly introduced to the paste, and the stirring process continued up to about 3 min until a homogenous mortar mixture was obtained. Furthermore, three additional mortar mixtures were produced that contained 10 % FCA activated with 6, 8, and 10 % $Na_2O$ having a lower w/p ratio based on the rheological study.

### 2.2. Experimental procedure

#### 2.2.1. Setting time

The initial and final setting times (in min) of AAP samples were measured using an automatic Vicat apparatus. The w/p ratio was kept constant as 0.30 for all investigated AAP mixes. The procedure explained in ASTM C191 was followed to evaluate the initial and the final setting times, excluding the determination of normal consistency and considering constant w/p ratio, and the results were reported nearest to 1 min. Eq. (1) was used to calculate the initial setting time of each AAP sample, whereas the final setting time was noted once the needle unable to puncture the AAP specimen.

$$Initialsettingtime = \left(\left(\frac{H-E}{C-D}\right)\times(C-25)\right)+E \quad (1)$$

In the equation, $H$ and $E$ represent the time of last penetration less than 25 mm and greater than 25 mm, respectively. $C$ and $D$ denote the penetration depth, in mm, at the time $E$ and $H$, respectively.

#### 2.2.2. Rheology

To examine the influence of FCA and $Na_2O$ dosage on the rheological properties of AAP samples, the mixtures containing 0, 10, 20, and 30 wt % FCA with $Na_2O$ dosages of 6, 8, and 10 wt% were produced. The samples containing 10 % FCA and activated 6 and 10 wt% of $Na_2O$ were also prepared with a reduced w/p ratio. Anton Paar's (ReolabQC) rotational rheometer, as shown in Fig. 1.a, was used to study the rheological characteristics. The analyses were conducted with a four-blade vane stirrer measuring system that has a length of 40 mm and a diameter of 11 mm. A strain-controlled system was employed and rheological parameters such as plastic viscosity and yield stress were determined. The rheological measurements were started with a constant pre-shear at 100 $s^{-1}$ for 30 s to homogenize the paste. After a rest of 30 *sec*, a stepped ramp up from 0.1 to 100 $s^{-1}$ and a stepped ramp down from 100 to 0.1 $s^{-1}$ were implemented on the specimens. The rheological procedure applied to pastes is shown in Fig. 1b. Each shear rate was applied long enough as 20 s to obtain steady-state shear stress for each shear rate value. The rheological behavior of pastes was investigated right after the mixing process and the test was continued at constant temperature of 20℃ using the temperature control unit of the rheometer.

The down curves of the shear stress-shear rate graphs were taken into account to calculate the yield stress and the plastic viscosity of the paste specimens. Flow and viscosity curves of the pastes were obtained via the software of the rheometer. Due to the Non-Newtonian relation between shear rate and shear stress, rheological parameters of AAP mixes were calculated by the Modified Bingham model (Eq.2). A good linear fit ($R^2$ greater than 0.98) was obtained between the shear stress and shear rate.

$$\tau = \tau_0 + \mu \times \dot{\gamma} + cx\dot{\gamma}^2 \quad (2)$$

In this equation, τ, $\tau_0$, and μ represent the shear stress (Pa), yield stress (Pa), and plastic viscosity (Pa.s), respectively. In addition, $c$ demonstrates the second-order parameter ($Pa.s^2$) and $\dot{\gamma}$ indicates shear rate.

#### 2.2.3. Semi-adiabatic test

The semi-adiabatic calorimeter test was carried out to monitor the temperature evolution and critical temperature-related parameters of a

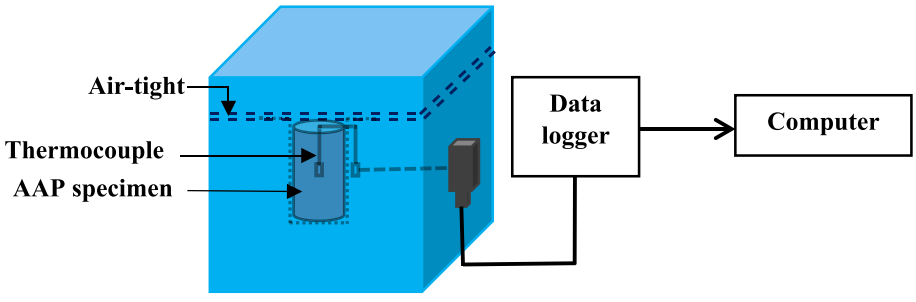



**Fig. 2.** The schematic illustration of the semi-adiabatic calorimetry test setup.

**Table 2**
The oxide components of FCA and BFS.

| Material | Composition (wt %) | | | | | | | | | | | | | | | |
|---|---|---|---|---|---|---|---|---|---|---|---|---|---|---|---|---|
| | MgO | $SiO_2$ | $Al_2O_3$ | $Cr_2O_3$ | $K_2O$ | ZnO | $Fe_2O_3$ | $Na_2O$ | CaO | MnO | $TiO_2$ | NiO | CuO | $P_2O_5$ | $SO_3$ | $Cl^-$ |
| FCA | 37.90 | 28.80 | 8.49 | 6.14 | 5.98 | 4.41 | 2.76 | 0.68 | 0.60 | 0.47 | 0.12 | 0.07 | 0.01 | 0.01 | 2.38 | 1 |
| BFS | 5.00 | 39.00 | 12.50 | – | 0.20 | – | 1.00 | 0.60 | 37.50 | 5.00 | – | – | – | – | 0.30 | – |

mixture, including time to reach the peak temperature and maximum exothermic temperature [33]. Fig. 2 depicts the schematic demonstration of the semi-adiabatic test setup and data collection process. The test setup was called semi-adiabatic calorimetry since some heat loss is expected to occur even though the enclosure is well insulated. Since the heat losses of the test setup depend on the ambient conditions, to avoid the different amounts of heat losses, the alkali activator solutions and powder materials were kept in a climate-controlled room at 22 ± 2 °C for 24 h before mixing. The semi-adiabatic tests were conducted on AAP samples produced with a w/p ratio of 0.30. The powder and alkaline solution were stirred in a mixer bowl for 3 min and subsequently poured into the cylinders of diameter 50 mm and height 100 mm, respectively. The mold was inserted into the insulating container, and a K-type thermocouple was immediately immersed into the fresh paste mixture. Temperature data were recorded for about 24 h in a climate-controlled room.

### 2.2.4. Compressive strength development

The compression test of AAM specimens was carried out on the 50 × 50 × 50 $mm^3$ cubic specimens. The mortar specimens were cured at a temperature of 22 ± 2 °C and relative humidity of 55 ± 2 %. Three specimens were tested for each mix at the curing age of 7, 28, and 56 days and the average values were noted.

### 2.2.5. Water absorption and voids content

Water absorption and the voids content of the AAM specimens were determined on the 50 × 50 × 50 $mm^3$ cubic samples. The specimens were oven-dried for 24 h at 60 °C instead at 110 ± 5 °C and the rest of the procedure was followed according to the method explained in ASTM C642. The reason behind selecting 60 °C to oven-dry the specimens was to avoid extreme desiccation of the binding phases caused due to thermal drying in alkali-activated slag-based binders [34].

### 2.2.6. Mass loss and drying shrinkage

The drying shrinkage and mass change measurements were performed on the AAM prisms with dimensions of 25.4 × 25.4 × 285 $mm^3$ following ASTM C596 standard. The mortar samples were demolded 24 h after casting, and the initial reading of length was taken with a length comparator. After the first length measurement, all prismatic samples were placed in a controlled chamber of temperature 22 ± 2 °C and relative humidity of 55 ± 2 %. The following measurements were taken at 2, 3, and 7 days of curing age, and consecutive measurements of the length changes were recorded on weekly periods up to 120 days. The reported data points presented in the drying shrinkage graphs represent the average value of the length change for two identical mortar specimens. Besides, mass of the mortar specimens were also measured before length change measurements.

### 2.2.7. Microstructure analysis

The AAP samples were produced in plastic tubes of a volume of 50 $cm^3$ to study the microstructure. The samples in sealed tubes were accumulated in ambient conditions at 22 ± 2 °C. The samples were soaked in acetone to terminate the reaction and proceeded for analysis at the age of 28 days.

The XRD analysis was conducted using a PANalytical X'Pert PRO diffractometer instrument to distinguish the crystalline patterns in the collected powder samples of the selected AAPs. The AAP samples were vacuum-impregnated with epoxy resin and cured for 24 h at laboratory temperature. Then, the surplus epoxy resin was removed by polishing the samples to obtain a plain and smooth surface. SEM observations in Back-Scattered Electron (BSE) mode were performed to analyze the microstructure and morphology of the AAP samples using Zeiss EVO® LS 10 SEM device equipped with energy-dispersive X-ray spectroscopy (EDS). In addition, elemental mapping was also employed on the specific area of the specimens to visualize and examine the element compositions and distributions.

## 3. Results and discussion

### 3.1. Characterization of raw materials

The chemical compositions obtained by X-ray fluorescence (XRF) analysis of the raw materials are presented in Table 2. Silicon and alumina are abundantly appear in both FCA and BFS. The ratio of $SiO_2$/$Al_2O_3$ in FCA and BFS are found as 3.39 and 3.12, respectively. Additionally, MgO and $Cr_2O_3$ are also found as major oxide components,

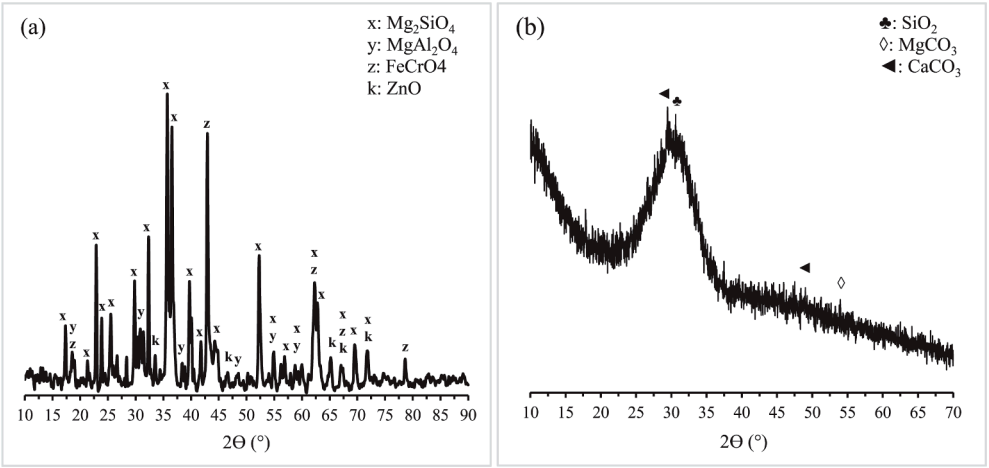



**Fig. 3.** XRD analysis of: (a) FCA and (b) BFS.

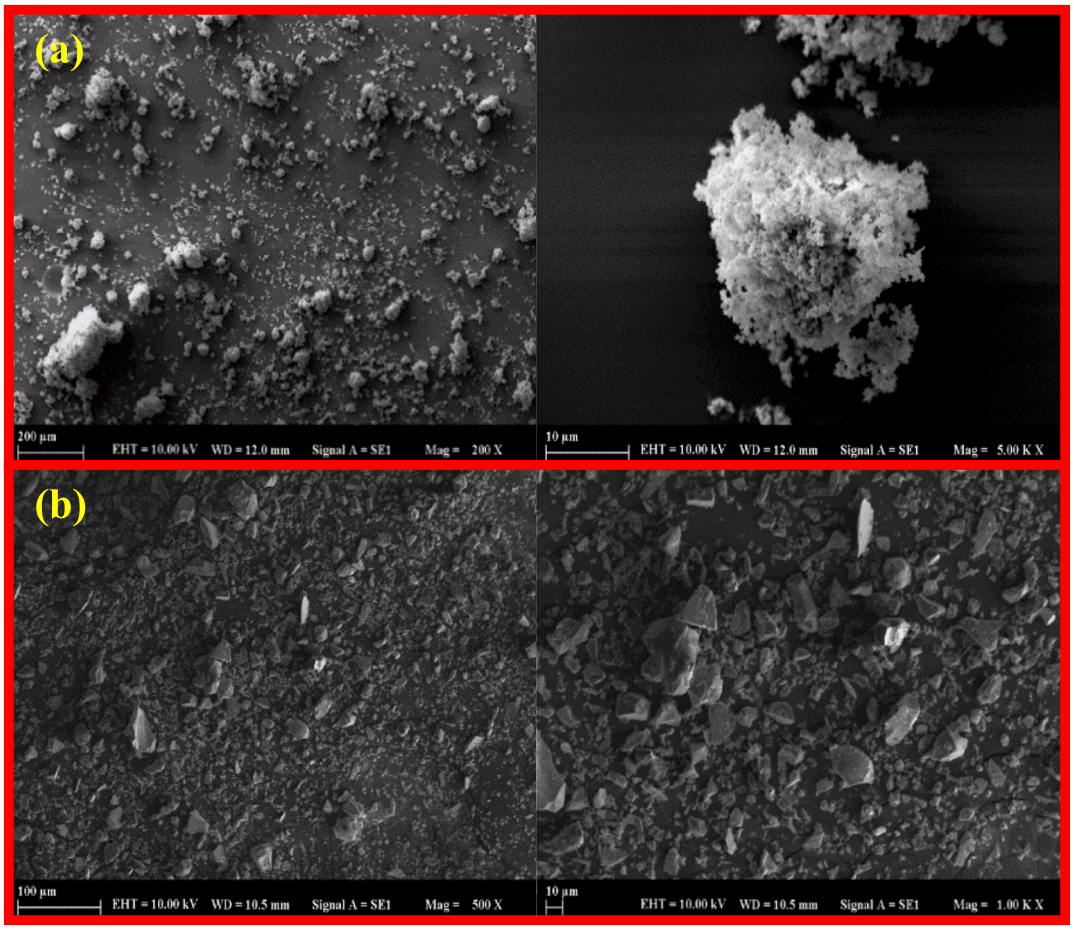



**Fig. 4.** SEM micrographs of: (a) FCA and (b) BFS.

whereas $K_2O$ and ZnO as minor in FCA. BFS contained a significant amount of CaO which was used as a calcium source material to blend with FCA. The other oxides were present in trace quantities in both raw materials. The XRD diffraction patterns of FCA and BFS are presented in Fig. 3. According to both chemical composition and XRD analysis, FCA is mainly composed of forsterite ($Mg_2SiO_4$) and spinel ($MgAl_2O_4$) phases, also lesser amounts of chromite ($FeCrO_4$) and zinc oxide (ZnO) phases. Similarly, BFS is distinguished by the presence of a broad diffused hump in the range between 25 and 35° 2Θ, corresponding to the amorphous phase. The primary crystalline patterns of quartz ($SiO_2$), magnesite ($MgCO_3$), and calcite ($CaCO_3$), are identified in BFS. Fig. 4 reflects the SEM images of FCA and BFS. The morphology of FCA particles is observed to be an agglomeration of very fine particles, whereas BFS particles were rather scattered and irregular in shape. Fig. 5 reveals the particle size distribution (PSD) of FCA and BFS. FCA particles were evidently coarser than BFS particles as reflected in SEM and PSD analysis. The average particle size ($d_{50}$) of FCA and BFS were obtained as 82.68 and 9.93 µm, respectively, whereas the maximum particle size was 316.22 and 45.6 µm, respectively.

### 3.2. Rheology

The outcome of various $Na_2O$ dosages and FCA replacement ratios on the rheological properties of AAP samples are shown in Figs. 6-7. The yield stress and plastic viscosity values obtained from the modified Bingham model are plotted in Fig. 6. It is evident that the rheological response of AAP samples strongly depends on the concentration of the alkaline activator. The investigated AAP mixtures exhibited plastic viscosity values ranging between 22.9 and 129.2 Pa.s. The higher $Na_2O$ content resulted in higher plastic viscosity regardless of FCA content, which is in line with the study conducted by Rifaai et al. [35] on alkali-activated slag mixes. The increase in plastic viscosity with increasing $Na_2O$ dosage can be credited to the high dissolution rate due to higher activator alkalinity that facilitated the rapid formation of gel reaction products [36,37]. In addition, the significant raise in plastic viscosity may also be attributed to the comparatively high viscosity of the alkaline solution with a higher $Na_2O$ dosage used [35,38]. The yield stress of the AAP mixtures varied between 40.7 and 89.8 Pa and an increase in the $Na_2O$ dosage from 6 % to 10 % resulted in a slight rise in yield stress.

In the alkali-activated blended systems, precursor type is another parameter that affects the rheological behavior of AAP. Yield stress and plastic viscosity are related to the flocculation of particles. The effect of flocculation on the rheological properties mainly depends on the shape, particle size distribution, and geometrical properties of the agglomerate structures, which further depend on the different dissolution degrees of Si and Al from the particle surface [39,40]. FCA addition had a beneficial effect on the rheological properties due to its distinct particle size distribution and particle shape compared to BFS. Since the FCA particles were coarser than BFS, the replacement of FCA might have provided a rise in free water content with the same w/p ratio. This situation led to a decrease in the yield stress and plastic viscosity of the pastes with increasing FCA amount. Additionally, the particle shape of FCA is comparatively spherical to that of BFS and sharp edges are not observed as shown in Fig. 4. Considering the contribution of FCA to the rheological properties, the mixes containing 10 % FCA activated with 6 and 10 % $Na_2O$ dosages were produced with a lower w/p ratio of 0.27. The trial tests indicated that P10-N6* and P10-N10* provided comparable rheological properties with P0-N6 and P0-N10, respectively, as shown in Fig. 6b and 7b. The positive influence of FCA on rheological properties was also considered in mortar mixes containing 10 % FCA and the w/p

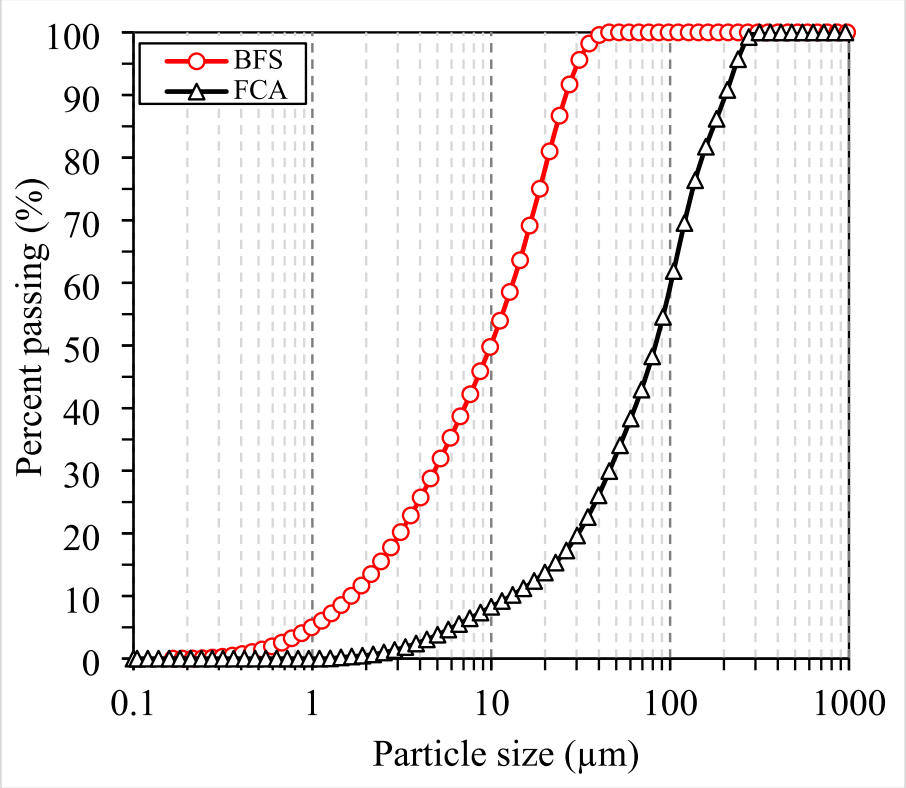



**Fig. 5.** PSD curves of FCA and BFS.

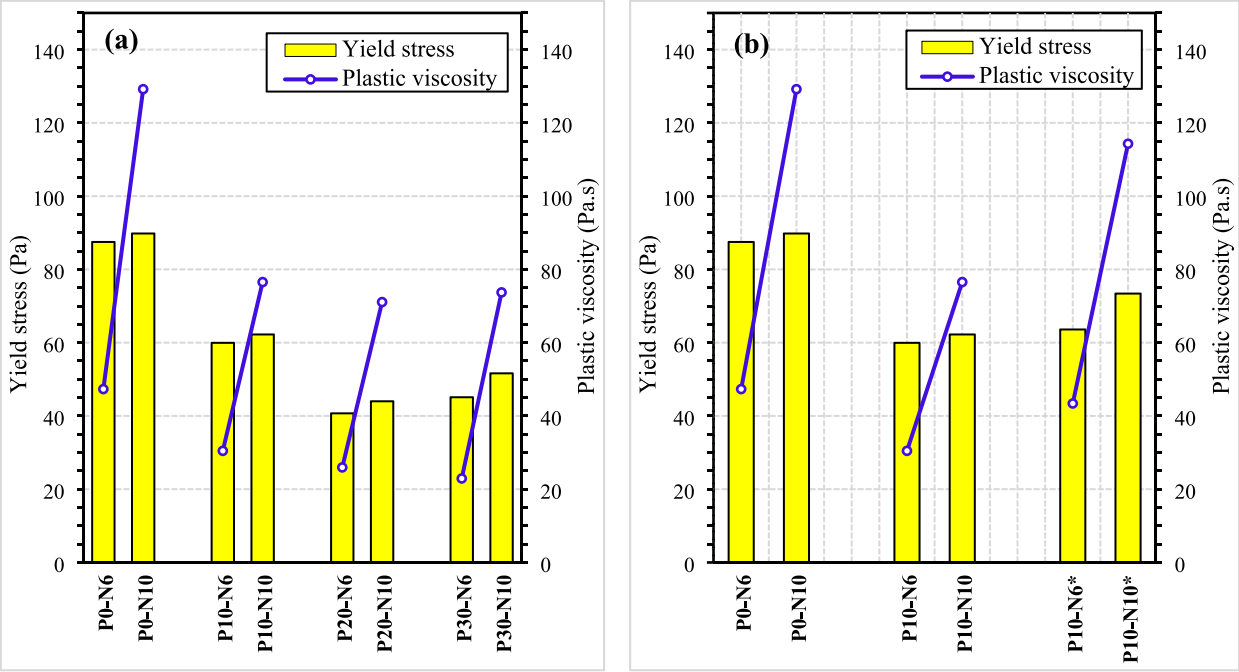



**Fig. 6.** Plastic viscosity and yield stress results of AAP mixtures.

ratio was reduced proportionally as in the paste to further investigate the contribution to physical and mechanical properties of mortars.

### 3.3. Setting time

Fig. 8 presents the impact of the FCA replacement level and $Na_2O$ dosage on setting time of the AAP samples. The setting time of AAP samples was significantly altered with the addition of FCA and a change in the $Na_2O$ dosage. The initial setting time of the AAP specimens ranged between 14 and 189 min, while the final setting time varied between 25 and 256 min, where the lowest values indicate the control AAP mixes without FCA. The increase in $Na_2O$ dosage from 6 to 10 % significantly

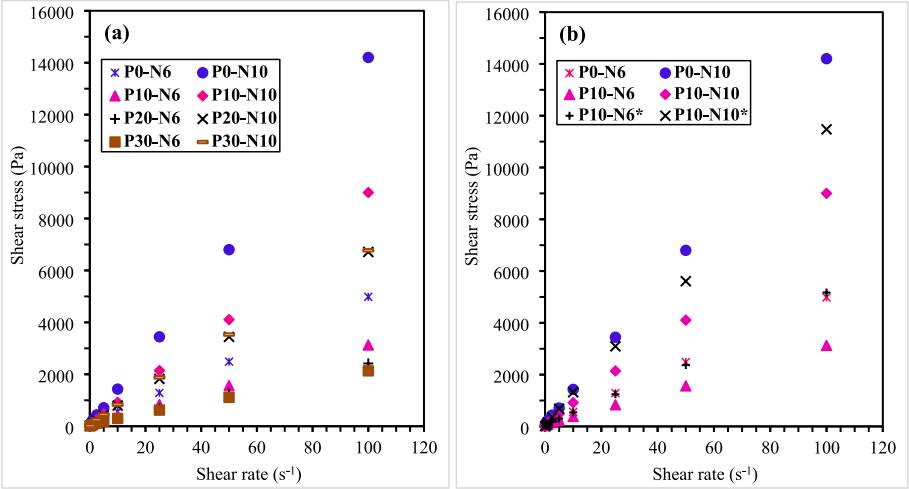



**Fig. 7.** Flow curves of AAP specimens.

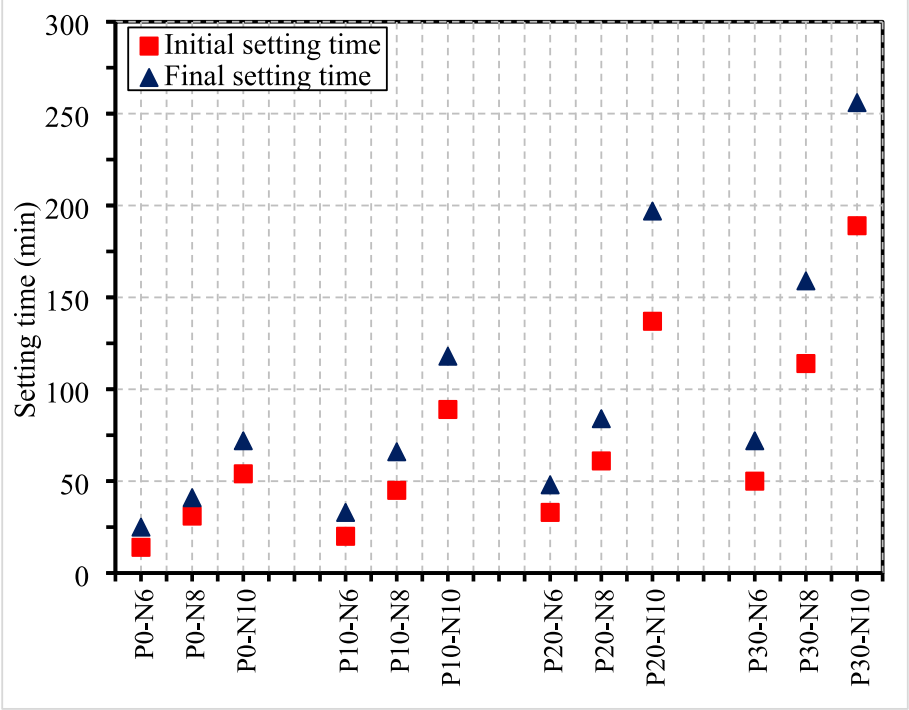



**Fig. 8.** The setting time results of AAP samples.

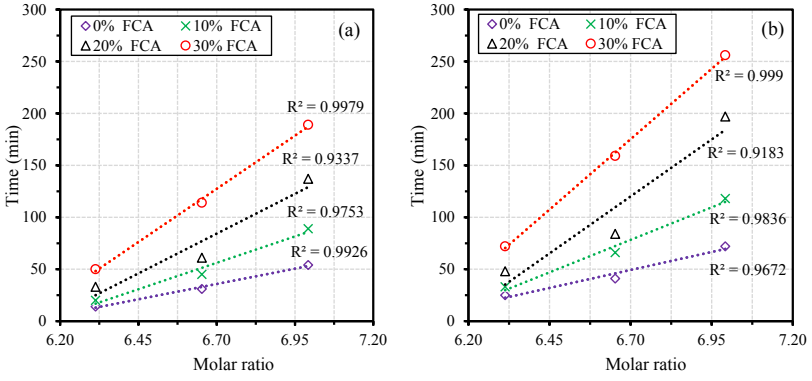



**Fig. 9.** The relationship between initial $SiO_2/Al_2O_3$ molar ratio with (a) initial setting time and (b) final setting time.

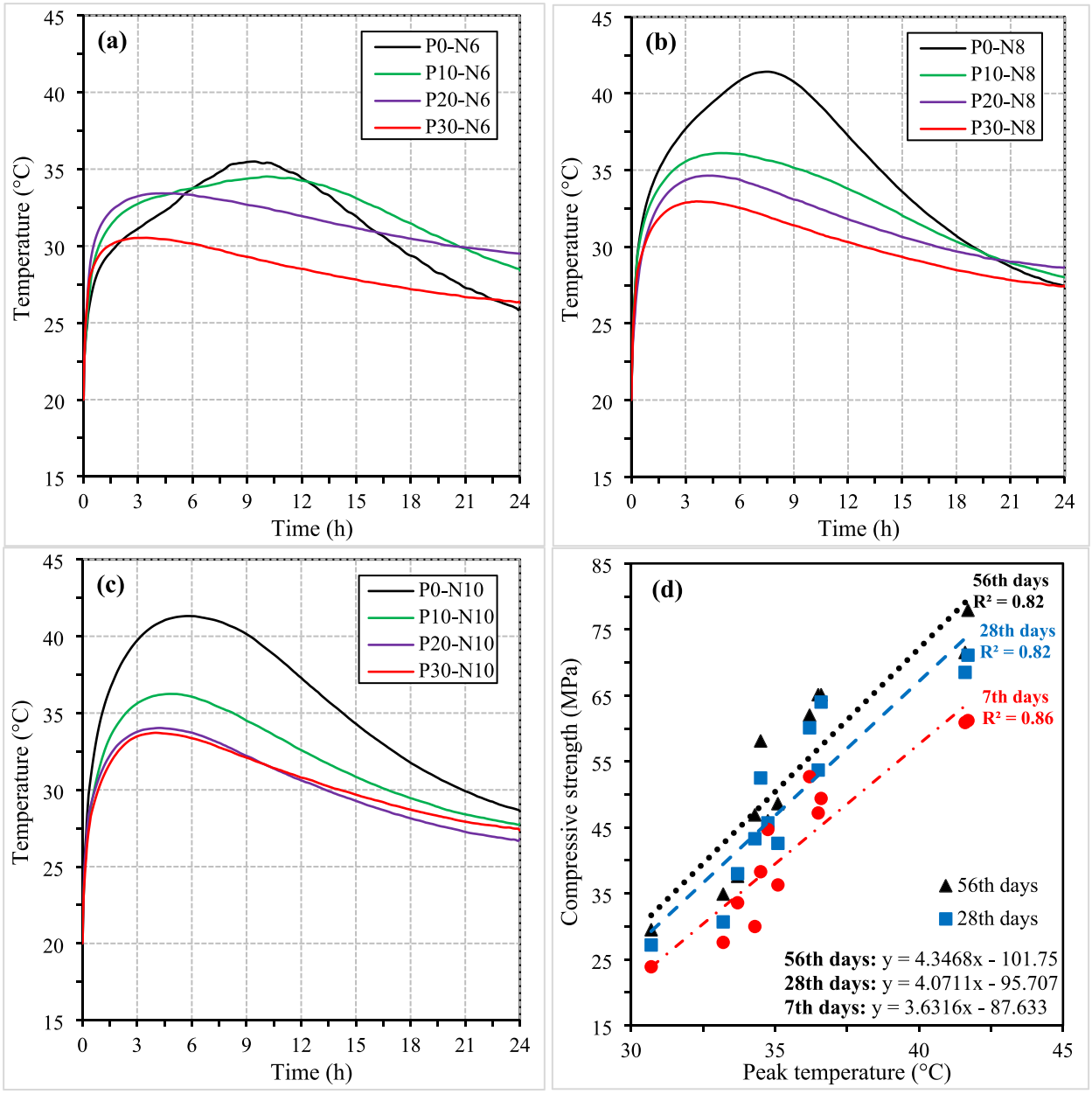



**Fig. 10.** The influence of FCA addition on the semi-adiabatic temperature profiles: (a) 6 % $Na_2O$, (b) 8 % $Na_2O$, and (c) 10 % $Na_2O$. (d) The relationship between peak temperature and 7, 28, and 56 days compressive strength.

increased the initial and final setting time by up to 345 % and 310 %, respectively. The prolonged initial and final setting time with higher $Na_2O$ dosage can be attributed to the higher dissolution degree of the BFS and FCA due to the high concentration of $OH^-$ ions during the early stage of hydration reactions [41]. The increase in FCA ratio from 0 to 30 % consistently extended the initial and final setting time by up to 268 % and 287 %, respectively. In other words, an increase in BFS (i.e., a decrease in FCA) reduced the setting time which can be credited to the rapid dissolution of Ca, Si, and Al due to the high reactivity of BFS under alkaline conditions that accelerates the formation of reaction products and the setting [42]. Zhu et al. [43] studied the initial setting time of AAPs using BFS obtained from different sources and activated with SS solution. They found that the initial setting time varied between 15 and 85 min and that the BFS composition was one of the significant factors affecting the setting time. Since the fast setting behavior of BFS based alkali-activated binders may limit their practical applications [44], the prolonged setting time with FCA incorporation may provide an advantage over the fast setting behavior of BFS. The relationship between the initial $SiO_2/Al_2O_3$ molar ratio and the setting time, illustrated in Fig. 9, shows that the increase in the initial molar ratio of $SiO_2/Al_2O_3$ prolonged the setting time which is in well compatible with the conventional alkali-activated materials reported by [45–48].

### 3.4. Semi-adiabatic calorimetry

The temperature kinetics of AAP mixes containing 6, 8, and 10 % of $Na_2O$ and 0, 10, 20, and 30 % replacement ratios of FCA monitored over a period of 24 h are illustrated in Figs. 10-11. It is worth mentioning that the paste specimen was mixed outside the semi-adiabatic instrument, the samples were then placed into the instrument and zero time began immediately after placing the specimens. The results showed that all temperature curves exhibited single peaks during the early stages of the reaction; following that, the temperature gradually decreased until it reached the ambient temperature. This phenomenon is a result of

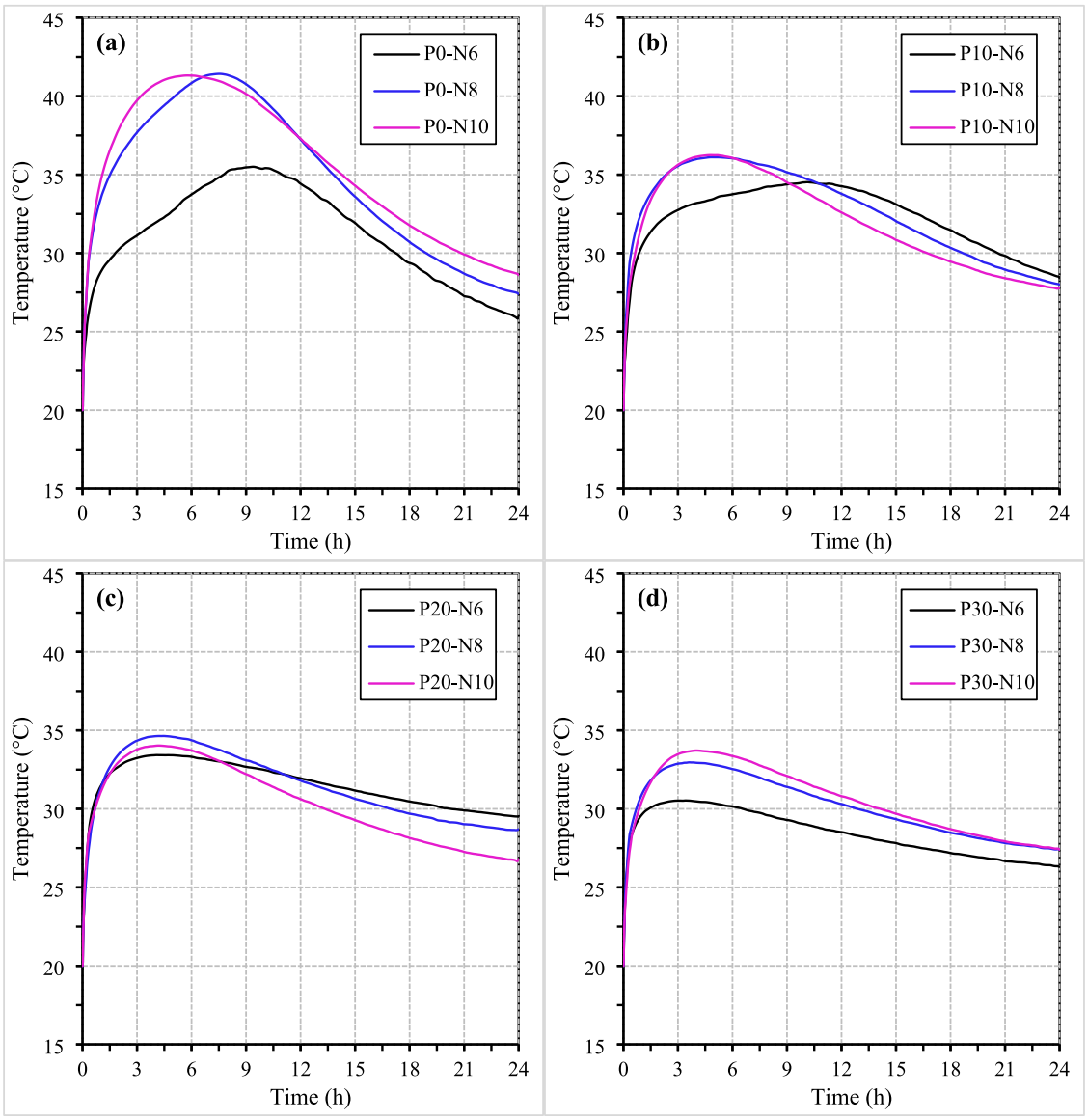



**Fig. 11.** The influence of $Na_2O$ dosage on the semi-adiabatic temperature profiles: (a) 0% FCA, (b) 10% FCA, (c) 20% FCA, and (d) 30% FCA.

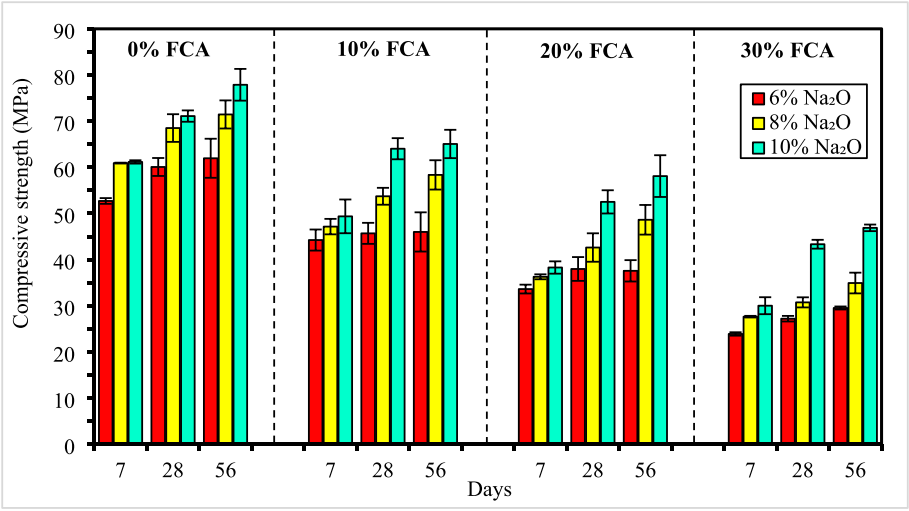



**Fig. 12.** The compressive strength of AAM specimens.

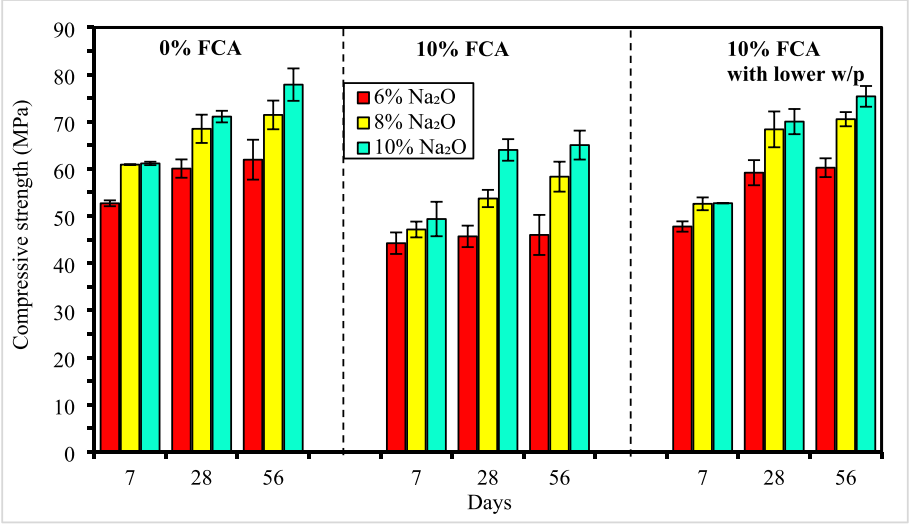



**Fig. 13.** The compressive strength comparison among AAM specimens containing 0 % FCA and 10 % FCA with w/p = 0.35 and 10 % FCA with w/p = 0.315.

particle wetting, the initiation of dissolution of the precursors, and the synthesis of aluminosilicate complexes [49]. As shown in Fig. 10, the AAP mixes without FCA had a higher peak temperature and an increase in FCA content progressively decreased the magnitude of the peak temperature. The highest exothermic peak temperature of 41.7 °C was observed in P0-N10, whereas P30-N6 had the lowest peak temperature of 30.7 °C, which is 26 % lower than that of P0-N10. The linear correlations were found between the semi-adiabatic peak temperature and the compressive strength as shown in Fig. 10d, in which the higher peak temperature corresponds to the higher compressive strength at both early and later ages.

The peak temperature generally increased with the increase in $Na_2O$ dosage as demonstrated in Fig. 11. For instance, the peak temperature of paste mixes activated with 10 % $Na_2O$ was found to be higher in the range between 2 and 15 % compared to the mixes with 6 % $Na_2O$, irrespective of the FCA content. The reason behind the higher peak temperature with decreasing amount of FCA and as well as with higher $Na_2O$ dosage can be due to the increased BFS content and higher alkalinity, respectively which promotes the quick dissolution of precursors followed by the development of exothermic polycondensation reactions [46,50]. The dissolution of BFS resulted in the formation of reaction products by providing enough dissolved silica and alumina to react with the CaO [51], influencing the peak temperature which also supports setting time results, that is an increase in FCA ratio extends setting and vice-versa. The paste mixtures containing FCA reached the peak temperature in a shorter period indicating that FCA incorporation slows down the hydration reactions. For example, the reference mixes without FCA achieved peak temperatures in the range between 344 and 543 min, whilst mixtures containing 30 % FCA were between 134 and 239 min.

### 3.5. Compressive strength

Fig. 12 plots the compressive strength test results of the AAM specimens and their variation depending on the $Na_2O$ dosage and FCA replacement ratios. In addition, Fig. 13 reveals the effect of reduced w/p ratios on the compressive strength of AAM samples containing 10 % FCA. The test results implied that an increased replacement ratio of FCA gradually reduced the compressive strength. Similar observations were reported by Kumar et al. [5]. AAM mixes incorporating 100 % BFS with 10 % $Na_2O$ dosage (M0-N10) exhibited the highest compressive strength of 79.1 MPa at 56 days. On the contrary, the lowest compressive strength value of 29.5 MPa at 56 days was observed for FCA30-N6. The

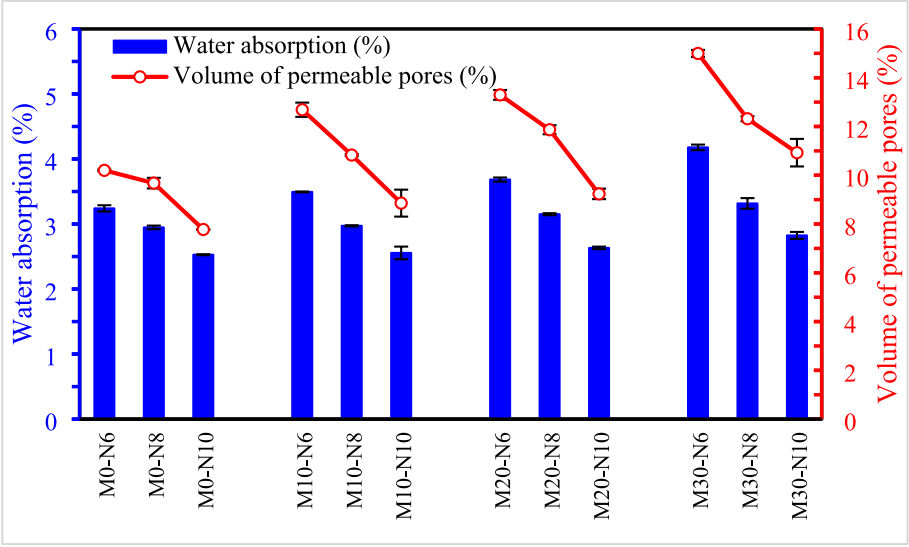



**Fig. 14.** The water absorption and VPP in hardened AAM specimens at 28 days.

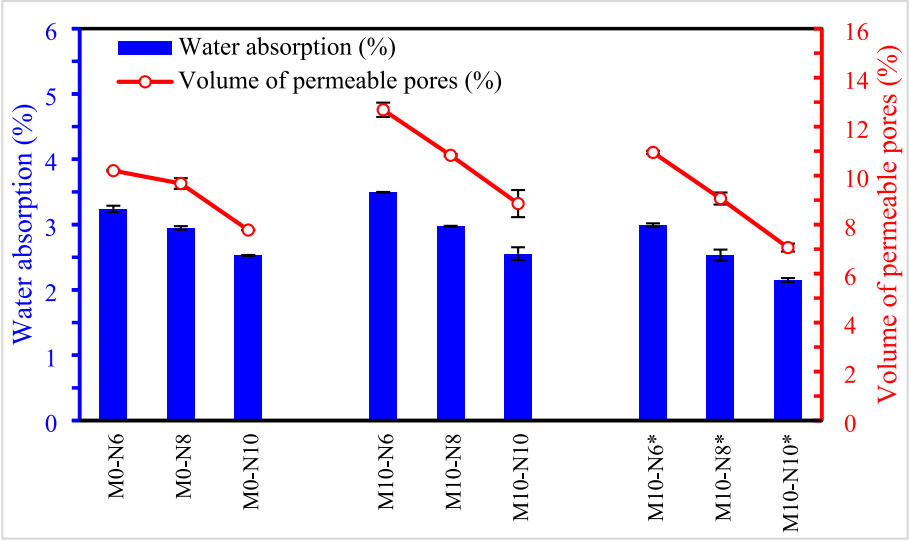



**Fig. 15.** The water absorption and VPP comparison among AAM specimens containing 0 % FCA and 10 % FCA with w/p = 0.35 and 10 % FCA with w/p = 0.315 at 28 days.

compressive strength of AAM is primarily related to the solvable calcium ions present in the precursor which involves the development of strength-giving gels such as C-A—S—H [52,53]. Hence, the reduction in compressive strength can be ascribed to the reduced calcium amount with increased FCA ratios which is also confirmed by SEM-EDS analysis (section 4.8.2).

It is also noteworthy that the increase in $Na_2O$ dosage significantly enhanced the compressive strength of mortar specimens in each FCA replacement series. The increase in $Na_2O$ content (i.e., higher alkalinity) subsequently leads to the generation of more hydroxide ions that causes increased dissociation of Si in addition to the release of Ca and hence increases the potential for the strength-giving reaction products formation [54,55]. Similarly, more SS is added with the increased $Na_2O$ dosage which might result in the generation of silica-rich products along with C—S—H gel which is also previously reported for the alkali-activated slag systems [56]. The effect of increased $Na_2O$ dosage from 6 to 10 % on the compressive strength was more pronounceable at 28 and 56 days compared to 7 days, particularly in the mixes with increased FCA content, as illustrated in Fig. 12. The 56-days compressive strength of AAM specimens comprising 0, 10, 20, and 30 % FCA consistently increased by approximately 26, 42, 55, and 59 %, with an increase in $Na_2O$ dosage from 6 to 10 %, respectively, denoting that the addition of FCA assists in compressive strength development at higher $Na_2O$ dosage.

The compressive strengths of the AAM specimens produced with 10 % FCA and lower w/p (i.e., w/p = 0.315) based on the rheological study were comparable to that of reference mixes without FCA manufactured with w/p of 0.35 at 28 and 56 days of curing age as revealed in Fig. 13. Furthermore, the compressive strengths of the 10 % FCA containing mixes with a w/p of 0.315 were higher in the range between 15.8 and 31.1 % compared to their counterpart mixes with a w/p ratio of 0.35.

### 3.6. Water absorption and volume of permeable pores

Fig. 14 demonstrates the variation of water absorption and volume of permeable pores (VPP) of AAM samples after 28 days of curing. The water absorption and VPP values of AAM samples both reduced noticeably with increasing $Na_2O$ dosage. On the contrary, the water absorption and VPP values gradually but slightly increased with an increase in the FCA replacement ratio. The water absorption and VPP values of the reference mortar produced with 100 % BFS varied between 2.5 % and 3.2 % and 7.8 %-10.2 %, respectively, and they ranged between 2.6 % and 4.2 % and 8.9–15 % for the FCA incorporated mixes, irrespective of $Na_2O$ dosage. The increase in water absorption and VPP might be due to the coarser particle size and lower reactivity of the FCA compared to BFS it replaced. Furthermore, the unreacted FCA particles might have modified the pore structure that might have caused increased water absorption and VPP. On the other hand, the use of finer FCA particles might be beneficial in reducing the water absorption and VPP by blocking the capillaries and modifying the pore structure, which requires further research. On the other hand, it can be noted that the effect of FCA content on the water absorption values of AAM samples was compensated with the high $Na_2O$ dosage of 8 and 10 %. For instance, the water absorption value of FCA0-N10 was obtained as 2.53 %, while mixtures containing 10, 20, and 30 % FCA with 10 % $Na_2O$ had

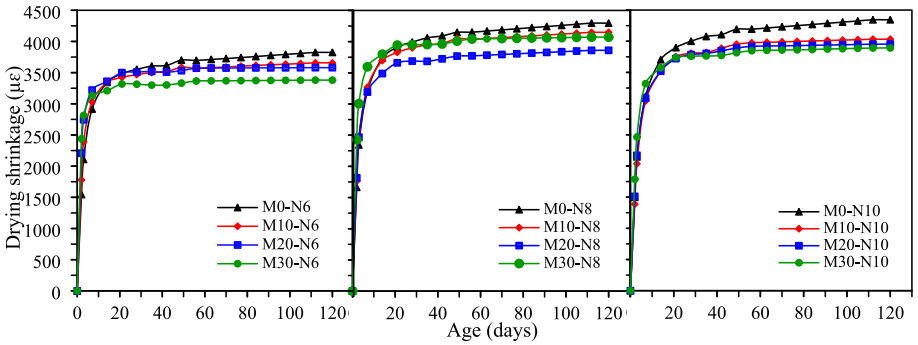



**Fig. 16.** The drying shrinkage behavior of AAM specimens.

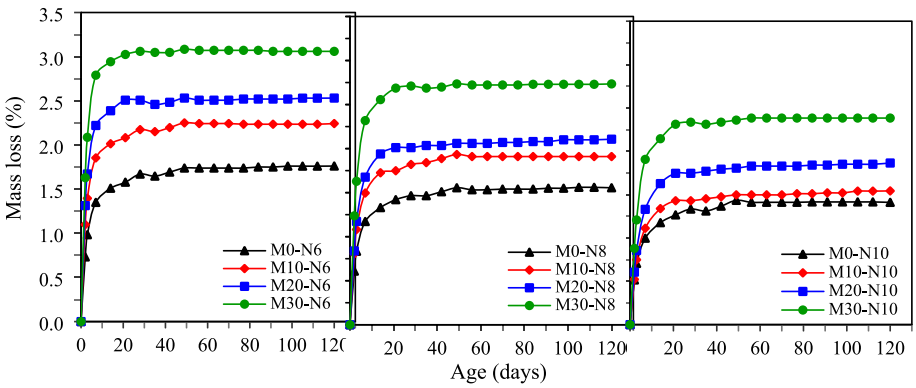



**Fig. 17.** The mass loss of AAM specimens.

water absorption values of 2.56, 2.63, and 2.82 %, respectively.

The water absorption and VPP results of AAM specimens produced with 10 % FCA and a lower w/p ratio of 0.315 are compared with the mortar samples incorporating 0 % and 10 % FCA with a w/p ratio of 0.35 in Fig. 15. It can be observed that the water absorption and VPP of AAM specimens manufactured with 10 % FCA and lower w/p were lower and comparable to that of reference mortars produced with 100 % BFS. Similarly, water absorption and VPP values of mortars with 10 % FCA with lower w/p were 0.4 to 0.5 % and 1.7 to 1.8 % lower, respectively, as compared to that of the same mixture with w/p of 0.35 as anticipated.

### 3.7. Drying shrinkage and mass loss

Fig. 16 depicts the drying shrinkage strain of the AAM samples monitored for 120 days. The drying shrinkage of the AAM mixtures varied in the range between 3380 and 4344 microstrains (με). The increased amount of FCA from 0 to 30 % resulted in decreased shrinkage strain values between 5.2 and 11.6 %, irrespective of the $Na_2O$ dosage. This might be due to the unreacted metallic particles such as Fe and Cr present in the FCA, also revealed by SEM analysis, which act as barrier to reduce shrinkage of FCA incorporated mortar samples. Similarly, Hongqiang et al. [57] noted that the unreacted coal gangue particles are wrapped in the alkali-activated slag mortar matrix and play a skeleton role to reduce the drying shrinkage. On the contrary, the drying shrinkage of AAM samples slightly increased with an increase in $Na_2O$ dosage from 6 to 8 %, and a further increase in $Na_2O$ dosage resulted in comparable drying shrinkage. The increase in drying shrinkage can be attributed to the increased amount of SS as $Na_2O$ dosage increased from 6 to 10 % which might have reduced mesopore volume and porosity, which influences the shrinkage owing to self-desiccation [58]. The rate of drying shrinkage enhanced with an increase in FCA content and was significantly rapid during the first 14 days. Drying shrinkage values of the AAM mixtures at 14 days reached about 85 to 95 % of the ultimate drying shrinkage values recorded at 120 days.

The mass loss values of the AAM samples ranged between 1.4 and 3.1 % as presented in Fig. 17. It is clearly noticed that the higher $Na_2O$ dosage results in lower mass loss values for all FCA replacement ratios. For instance, the increase in $Na_2O$ dosage from 6 to 10 % reduced the

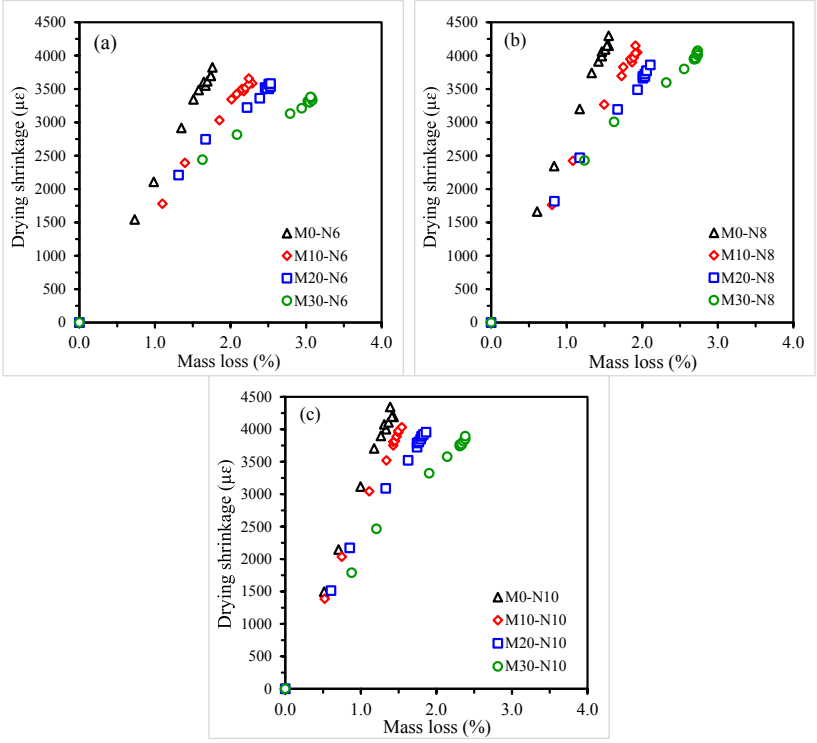



**Fig. 18.** The correlation between mass loss and drying shrinkage values of AAM specimens.

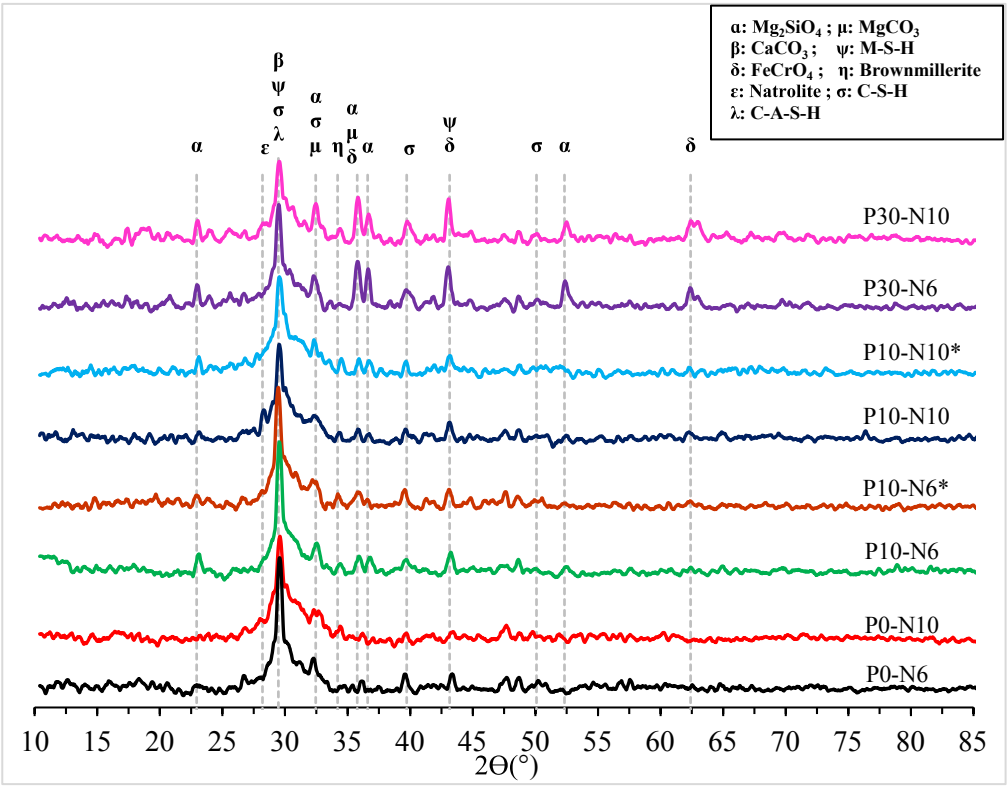



**Fig. 19.** XRD patterns of AAP samples.

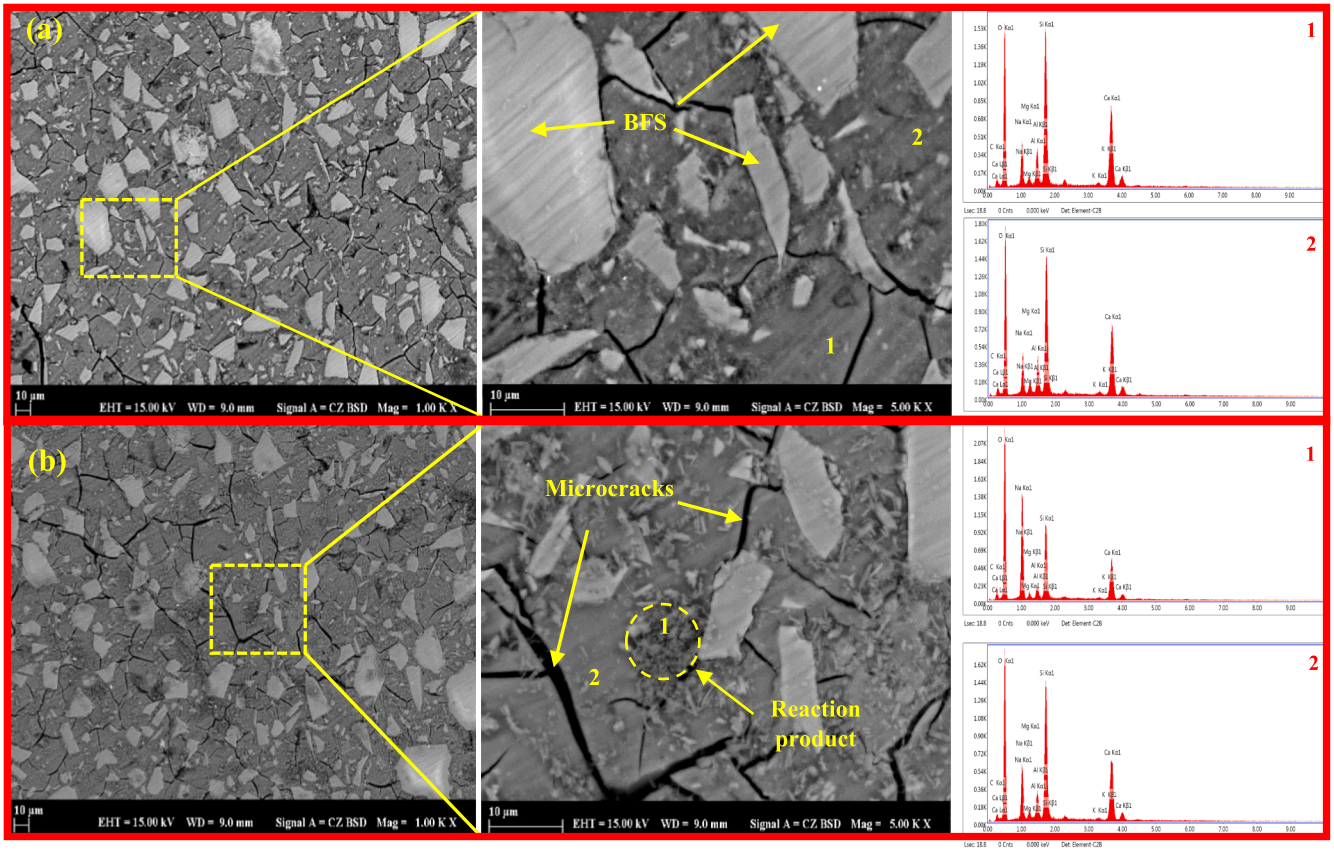



**Fig. 20.** BSEM and EDS of (a)P0-N6 and (b) P0-N10.

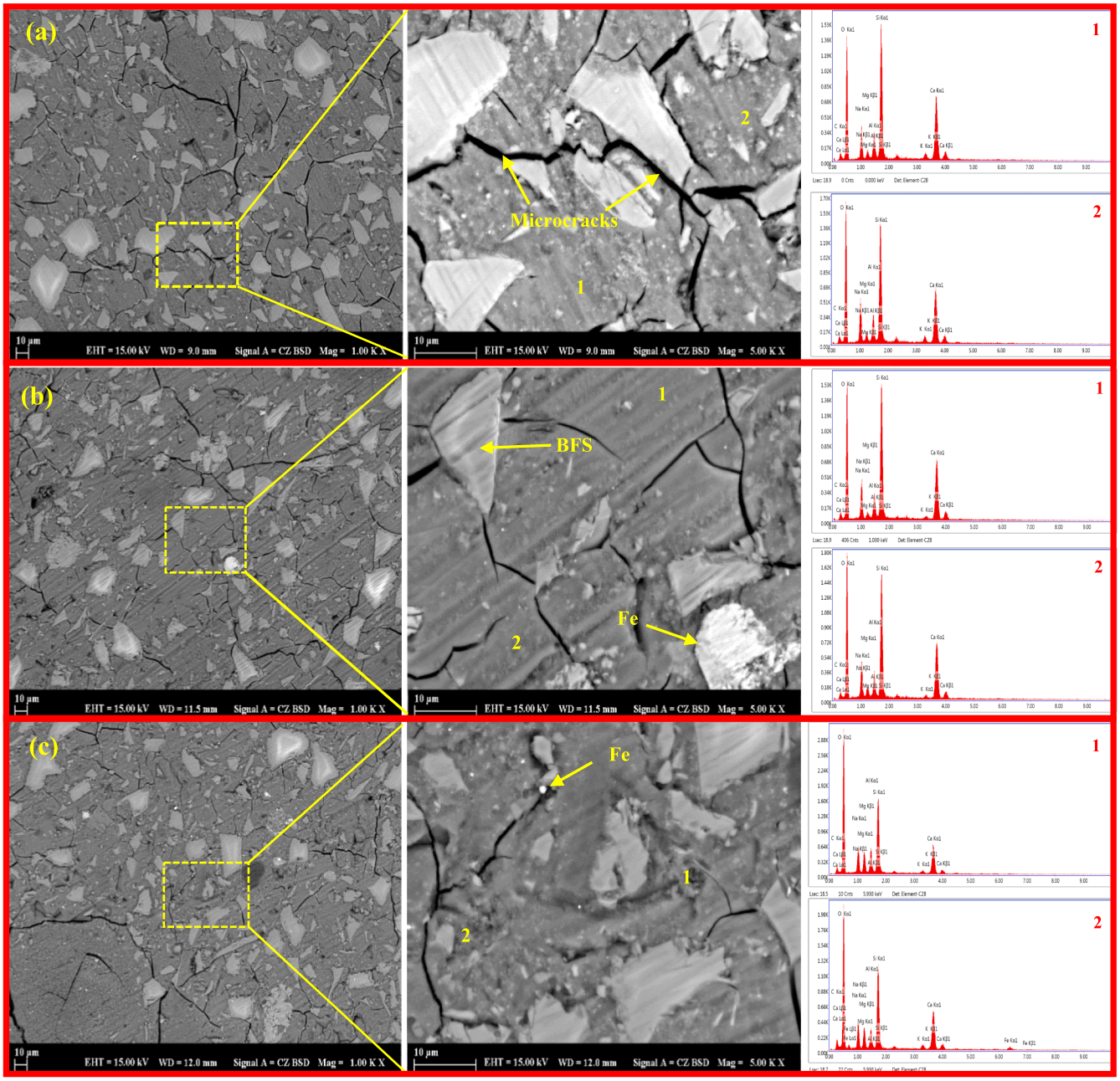



**Fig. 21.** BSEM and EDS of (a) P10-N6, (b) P10-N10, and (c) P10-N6*.

mass loss values between about 21 and 31 %. Additionally, FCA content notably affected the mass loss values of AAM mixes, as higher inclusion of FCA led to higher mass loss. This is in agreement with the VPP results discussed in Section 4.6, as FCA incorporation increased the open pores and resulted in higher mass loss which might be due to the modification of pore structure. Although higher mass loss, the drying shrinkage of FCA incorporated samples unexpectedly reduced. As previously noted, the reason for this might be due to the unreacted metallic particles that constraint the length change of samples which suppresses the shrinkage due to mass loss.

The correlations between drying shrinkage and mass loss measured at 120th days of the AAM samples are presented in Fig. 18. The drying shrinkage and mass loss seem to be concluded for the mixes containing FCA. However, the shrinkage of reference AAM samples without FCA continued, although little mass loss was observed which can be due to carbonation [20].

### 3.8. *Microstructural properties*

#### 3.8.1. *XRD analysis*

The XRD patterns of the investigated AAP samples are presented in Fig. 19. The major crystalline components were identified as C-A—S—H, C—S—H, and M—S—H. Additionally, traces of $CaCO_3$, brownmillerite, and natrolite were also observed. The higher calcium content of BFS compared to FCA contributed to the constitution of reaction products such as C-A—S—H and C—S—H. Such observations reasonably agree with the temperature flow recorded during the semi-adiabatic test; the increase in BFS ratio accelerates the polycondensation reaction and vice versa which might affect the resulting generation of reaction products. The crystalline composition of forsterite ($Mg_2SiO_4$), iron chromate ($FeCrO_4$), and spinel ($MgAl_2O_4$) which previously existed in FCA powder can also be observed in the AAP synthesized with FCA and BFS. The presence of abundant magnesium and low calcium in FCA might have

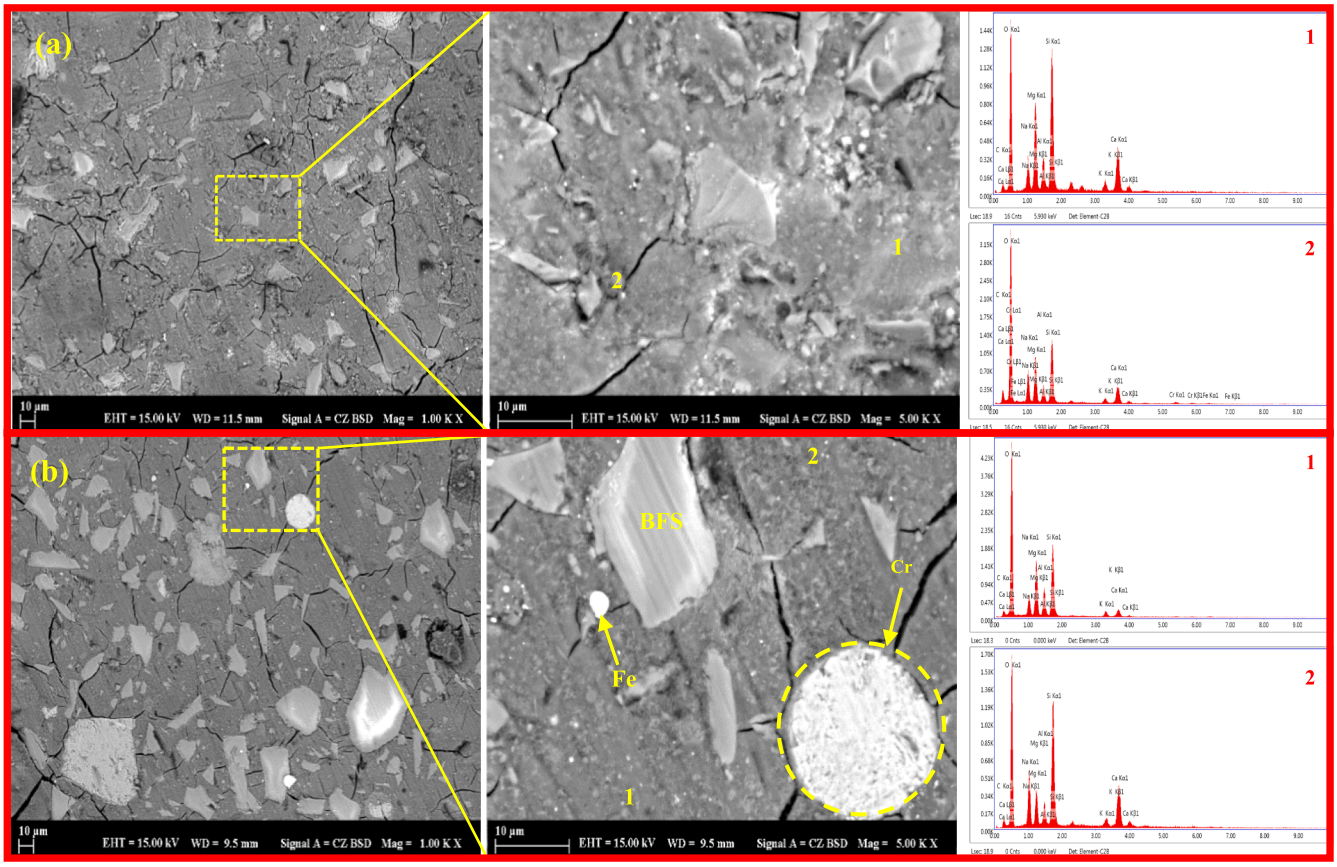



**Fig. 22.** BSEM and EDS of (a) P30-N6 and (b) P30-N10.

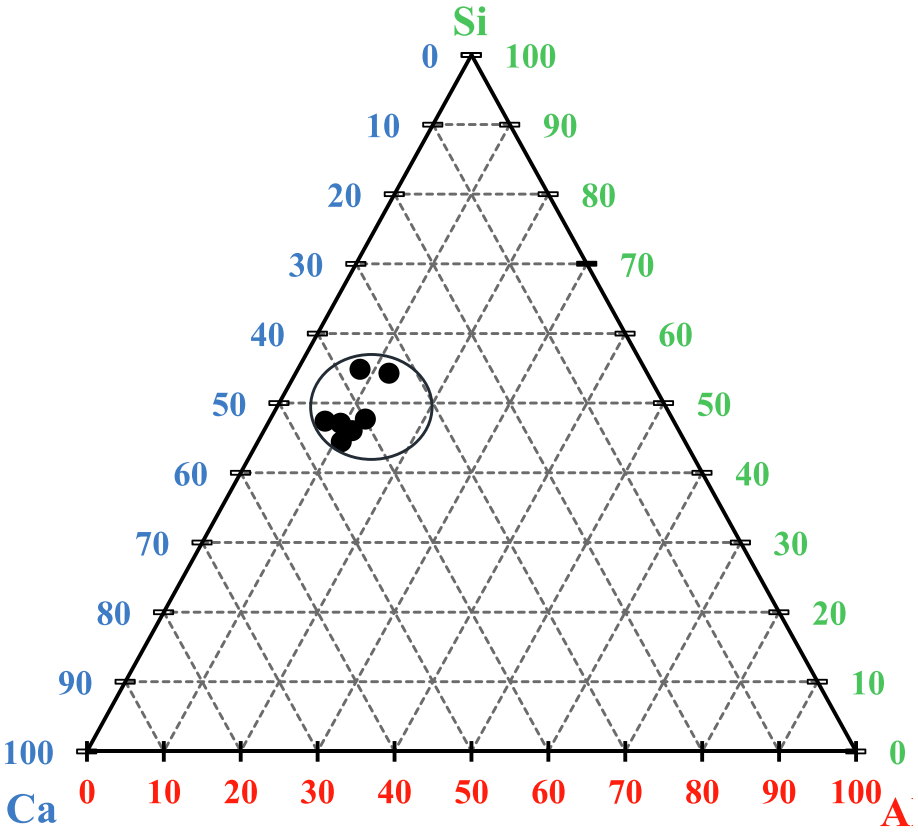



**Fig. 23.** Ternary representation of normalized Ca, Si, and Al obtained from EDS data for analyzed AAP.

**Table 3**
The average Ca/Si and Si/Al ratios of AAP samples and their corresponding mortar compressive strength at 28 days.

| Mix ID | Ca/Si | Si/Al | 28-day compressive strength of mortar (MPa) |
|---|---|---|---|
| P30-N6 | 0.59 ± 0.05 | 2.95 ± 0.57 | 27.2 ± 0.6 |
| P30-N10 | 0.68 ± 0.22 | 3.86 ± 0.11 | 43.3 ± 1.0 |
| P10-N6 | 0.92 ± 0.01 | 4.00 ± 0.46 | 45.7 ± 2.3 |
| P10N-6* | 0.94 ± 0.04 | 3.99 ± 0.27 | 59.2 ± 2.7 |
| P0-N6 | 1.01 ± 0.04 | 4.55 ± 0.07 | 60.1 ± 1.9 |
| P10-N10 | 0.94 ± 0.02 | 5.23 ± 0.34 | 64.0 ± 2.3 |
| P0-N10 | 1.46 ± 0.05 | 6.80 ± 0.10 | 71.1 ± 1.2 |

resulted in the generation of M—S—H which can be observed around 29.5° and 43.2° (2θ) and also verified in SEM-EDS analysis which represents peaks associated with Mg in the gel phase with increased FCA ratio, indicating the possible formation of M—S—H.

The diffraction peak of natrolite ($Na_2Al_2Si_3O_{10}·2H_2O$) was observed around 28° (2Θ), particularly in the AAP mixes incorporating FCA and activated with 10 % of $Na_2O$ dosage. The natrolite peak slightly intensified with increasing FCA ratios as seen in P10-N10 and P30-N10 compared to the P10-N6 and P30-N6, respectively attributing to the hydration reaction of FCA. Furthermore, the 28-day compressive strength of M10-N10 was relatively greater by about 40 % compared to M10-N6, whereas M30-N10 had approximately 59.2 % higher strength relative to M30-N6. This shows that the increase in $Na_2O$ dosage from 6 to 10 % was more effective in enhancing the compressive strength of AAM samples containing 30 % FCA compared to specimens with 10 % FCA. It can be inferred that the AAM samples containing an increased amount of FCA could participate in a hydration reaction that may facilitate the formation of natrolite in the mixes with higher $Na_2O$ dosage.

### 3.8.2. SEM/EDS analysis

Figs. 20-22 illustrate the back-scattered electron microscopy (BSEM) images along with the EDS results at various spots of the selected 28-day cured AAP samples with magnifications of × 1000 and × 5000. It was taken into account that the visible analysis area included reacted/unreacted FCA and BFS particles along with the matrix phase to detect reaction products during the EDS analysis. The morphology of unreacted BFS and FCA particles can be distinguished in the homogenous microstructure of the corresponding investigated AAP specimens. It can be noticed that the irregular light gray regions are the non-spherical BFS particles scattered throughout the microstructure. The continuous dark gray areas correspond to C-A—S—H or C—S—H gels observed in EDS analyses as the main binding phase, which were previously identified by XRD. In addition, unreacted Fe and Cr elements were also detected in the AAP samples containing 10 and 30 % of FCA. The dissolved ionic compounds present in FCA such as Fe and Cr particles were seen entrenched inside the matrix which could play a significant role in filling space.

The normalized calcium, silicon, and aluminum content obtained from EDS results for multiple points excluding unreacted precursor particles are plotted in Fig. 23. The ternary plot shows a clustered region of points indicating the formation of C-A—S—H type gel [17,59]. The average atomic ratios of Ca/Si and Si/Al varied in the range between 0.59 and 1.46 and 2.95–6.80, respectively as presented in Table 3. In addition, Fig. 24 depicts the correlation between the compressive strength of AAM specimens and their corresponding Ca/Si or Si/Al atomic ratios. In general, the increasing mechanical strength of AAM specimens showed a significant relationship with rising Ca/Si and Si/Al ratios with $R^2$ values of 0.85 and 0.90, respectively, which is consistent with increasing BFS ratios and $Na_2O$ dosage, indicating the higher formation of strength-giving reaction products. The generation of calcium silicate gels was evidently encouraged with a higher amount of Ca/Si and Si/Al atomic ratios which might have assisted in filling the voids and positively affected compressive strength and water absorption in samples activated with higher $Na_2O$ dosage.

The elemental distributions of the analyzed AAP specimens are presented in Fig. 25. The Al, Si, and O distribution in the elemental mapping intensify where BFS particles are located. In addition, less Na concentration proves that the darker areas are BFS particles surrounded by the paste. Other elements show a relatively homogenous distribution throughout the structure. On the other hand, since one of the main constituents of FCA is Mg as previously identified in XRD and observed in Fig. 24, especially increased Mg concentration in the elemental mapping demonstrated the increased amount of FCA. Besides, some white spots, which have relatively bigger particle sizes compared to the $MgSiO_4$ phase, were also found in P30-N10 and P10-N10 samples as observed in EDS and elemental analysis. The EDS spot analysis of these spots displayed that they can be metallic iron, iron oxide, or iron chromate which were also detected in the XRF and XRD analysis of raw

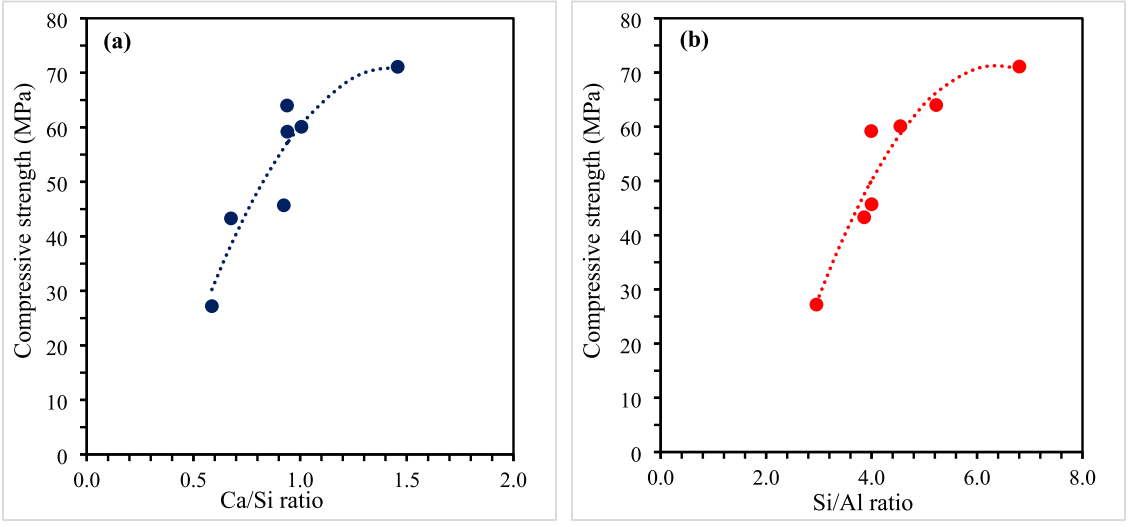



**Fig. 24.** The relationship between compressive strength and (a) Ca/Si ratio and (b) Si/Al ratio.

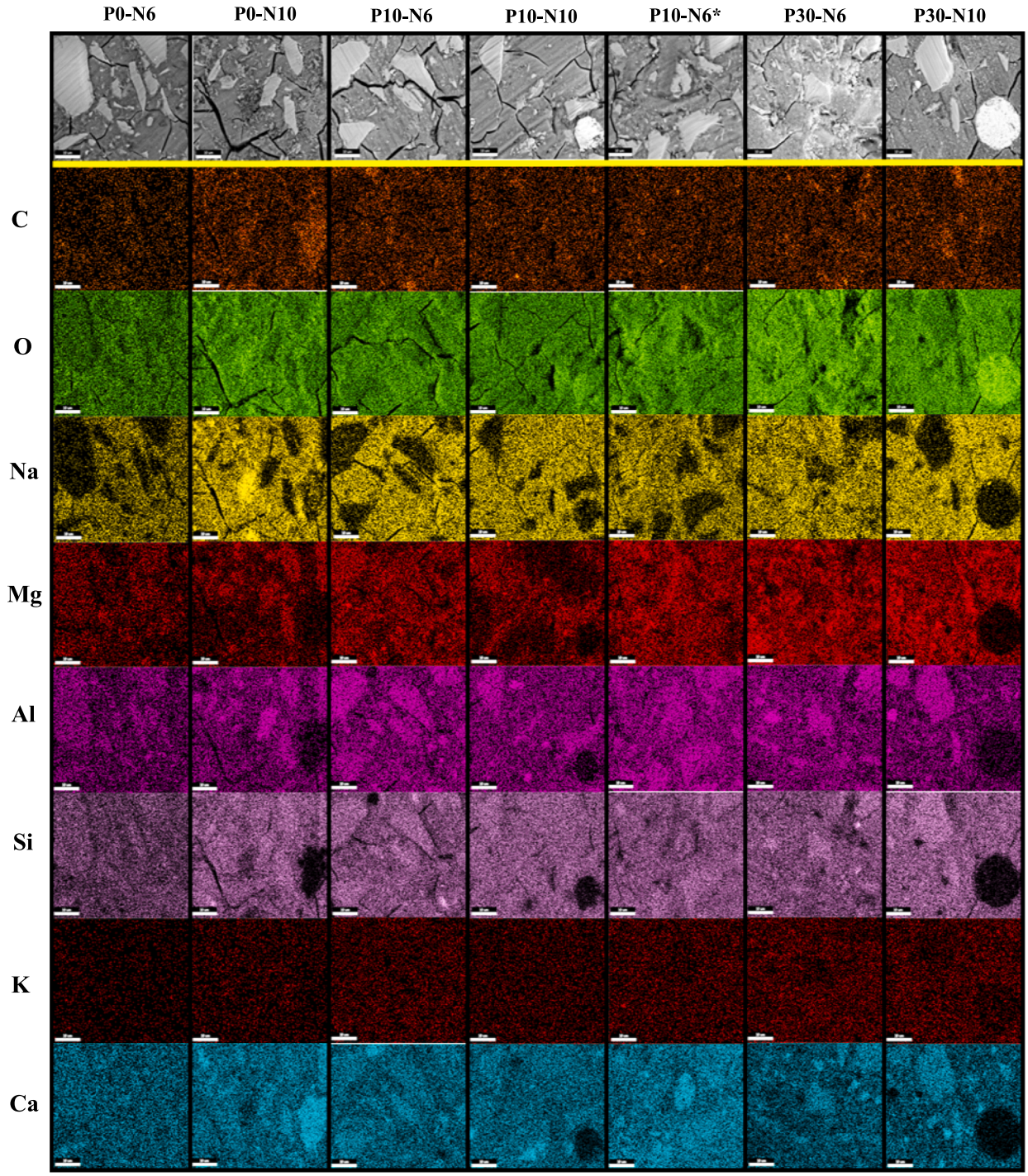



**Fig. 25.** Elemental distribution of AAP specimens.

FCA.

## 4. Conclusions

In this work, AAP and AAM samples were produced by activating BFS and FCA with a mixture of NaOH and SS to study the influence of various FCA replacement ratios on the fresh, physicomechanical, and microstructural properties. The key conclusions obtained from the study are listed below:

- The plastic viscosity and yield stress of the pastes ranged between 22.9 and 129.2 Pa.s and 40.7 and 89.8 Pa, and the inclusion of FCA significantly reduced the plastic viscosity and yield stress enabling a lower w/p ratio with comparable rheological properties. The increase in $Na_2O$ dosage induced higher plastic viscosity and moderately altered the yield stress of the AAP mixes.
- The increase in $Na_2O$ dosage and FCA replacement ratios significantly prolonged both initial and final setting times up to 345 % and 310 %, and 268 % and 287 %, respectively, compared to the reference mixes without FCA. The setting time of AAPs demonstrated a significant relationship with the initial $SiO_2/Al_2O_3$ molar ratio with $R^2$ greater than 0.90.
- The semi-adiabatic test results revealed that the peak temperature and time to peak temperature of AAP reduced with increasing FCA

content by up to about 20 % and 61 %, respectively. On the other hand, the increase in $Na_2O$ dosage generally led to a rise in peak temperature.

- The compressive strength of AAM mixes was consistently reduced with an addition of FCA, however, the increase in $Na_2O$ dosage significantly ameliorated the compressive strength of AAM samples. While the 56 day compressive strength of reference mix without FCA varied between 62.0 and 77.9 MPa, the 56 day compressive strength of 10 %, 20 %, and 30 % FCA containing mixes varied between 46.0 and 65.1 MPa, 37.6–58.1 MPa, and 29.5–46.9 MPa, respectively. Furthermore, significant and positive linear relationships were established between the peak temperature and compressive strength with $R^2$ values greater than 0.82.
- The water absorption and VPP values of the AAM specimens slightly increased with an increase in FCA content but significantly reduced with increasing $Na_2O$ dosage.
- The AAM produced with a reduced w/p of 0.315 showed comparable compressive strength, water absorption and VPP to that of reference mortar mixes with a w/p ratio of 0.35.
- Drying shrinkage of AAM mixes generally decreased with the higher addition of FCA. In contrast, the increase in $Na_2O$ dosage from 6 to 8 % led to an increment in drying shrinkage. Further increase in $Na_2O$ dosage insignificantly altered drying shrinkage.
- According to the microstructural and mineralogical investigations, the major hydration products of the AAP mixes were found as C—S—H, C-A—S—H, and M—S—H gels as well as forsterite, natrolite, brownmillerite, and spinel. The formation of M—S—H type gels were identified in mixes containing higher amounts of FCA.
- Ca/Si and Si/Al ratios governed the polymerization of major reaction products, and the increase in both ratios resulted in higher compressive strength.

## CRediT authorship contribution statement

**Tarik Omur:** Investigation, Data curation, Writing – original draft, Software, Validation. **Nausad Miyan:** Software, Data curation, Writing – original draft, Validation. **Nihat Kabay:** Supervision, Conceptualization, Methodology, Writing – review & editing, Validation. **Burak Birol:** Resources, Investigation, Writing – original draft, Validation. **Didem Oktay:** Investigation, Validation, Writing – original draft.

## Declaration of Competing Interest

The authors declare that they have no known competing financial interests or personal relationships that could have appeared to influence the work reported in this paper.

## Data availability

Data will be made available on request.

## Acknowledgment

This study was conducted at the Construction Materials Laboratory of Yildiz Technical University. The authors would like to thank Eti Krom A.Ş. Elazığ, Turkey, for supplying the ferrochrome ash used in the present work.

## References

[1] I. Capasso, B. Liguori, C. Ferone, D. Caputo, R. Cioffi, Strategies for the valorization of soil waste by geopolymer production: An overview, J. Clean. Prod. 288 (2021) 125646.
[2] P.K. Acharya, S.K. Patro, Use of ferrochrome ash (FCA) and lime dust in concrete preparation, J. Clean. Prod. 131 (2016) 237–246.
[3] J.J. Coetzee, N. Bansal, E.M.N. Chirwa, Chromium in environment, its toxic effect from chromite-mining and ferrochrome industries, and its possible bioremediation, Expo Health. 12 (1) (2020) 51–62.
[4] J. Mishra, S.K. Das, R.S. Krishna, B. Nanda, S.K. Patro, S.M. Mustakim, Synthesis and characterization of a new class of geopolymer binder utilizing ferrochrome ash (FCA) for sustainable industrial waste management, Mater. Today:. Proc. 33 (2020) 5001–5006.
[5] C. Kumar, S.C. Yaragal, B.B. Das, Ferrochrome ash–Its usage potential in alkali activated slag mortars, J. Clean. Prod. 257 (2020), 120577.
[6] P.K. Acharya, S.K. Patro, Utilization of ferrochrome wastes such as ferrochrome ash and ferrochrome slag in concrete manufacturing, Waste Manag.. Res. 34 (8) (2016) 764–774.
[7] P.K. Acharya, S.K. Patro, Effect of lime and ferrochrome ash (FA) as partial replacement of cement on strength, ultrasonic pulse velocity and permeability of concrete, Constr. Build. Mater. 94 (2015) 448–457.
[8] W. Lin, F. Zhou, W. Luo, L. You, Effect of alkali cation type on compressive strength and thermal performance of the alkali-activated omphacite tailing, Constr. Build. Mater. 306 (2021), 124647.
[9] N. Kabay, N. Miyan, H. Özkan, Utilization of pumice powder and glass microspheres in cement mortar using paste replacement methodology, Constr. Build. Mater. 282 (2021), 122691.
[10] H. Mikulčić, J.J. Klemeš, M. Vujanović, K. Urbaniec, N. Duić, Reducing greenhouse gasses emissions by fostering the deployment of alternative raw materials and energy sources in the cleaner cement manufacturing process, J. Clean. Prod. 136 (2016) 119–132.
[11] P.K. Acharya, S.K. Patro, Acid resistance, sulphate resistance and strength properties of concrete containing ferrochrome ash (FA) and lime, Constr. Build. Mater. 120 (2016) 241–250.
[12] N. Kabay, M. Mert, N. Miyan, T. Omur, Pumice as Precursor in Geopolymer Paste and Mortar, J. Civil Eng. Construct. 10 (2021) 225–236.
[13] F. Colangelo, I. Farina, M. Travaglioni, C. Salzano, R. Cioffi, A. Petrillo, Eco-efficient industrial waste recycling for the manufacturing of fibre reinforced innovative geopolymer mortars: Integrated waste management and green product development through LCA, J. Clean. Prod. 312 (2021), 127777.
[14] I. Amer, M. Kohail, M.S. El-Feky, A. Rashad, M.A. Khalaf, A review on alkali-activated slag concrete, Ain Shams Eng. J. 12 (2) (2021) 1475–1499.
[15] J. Ren, L. Zhang, R. San Nicolas, Degradation process of alkali-activated slag/fly ash and Portland cement-based pastes exposed to phosphoric acid, Constr. Build. Mater. 232 (2020), 117209.
[16] S. Aydın, B. Baradan, Sulfate resistance of alkali-activated slag and Portland cement based reactive powder concrete, J. Build. Eng. 43 (2021), 103205.
[17] I. Ismail, S.A. Bernal, J.L. Provis, R. San Nicolas, S. Hamdan, J.S.J. van Deventer, Modification of phase evolution in alkali-activated blast furnace slag by the incorporation of fly ash, Cem. Concr. Compos. 45 (2014) 125–135.
[18] X. Gao, Q.L. Yu, H.J.H. Brouwers, Reaction kinetics, gel character and strength of ambient temperature cured alkali activated slag–fly ash blends, Constr. Build. Mater. 80 (2015) 105–115.
[19] S. Samantasinghar, S. Singh, Effects of curing environment on strength and microstructure of alkali-activated fly ash-slag binder, Constr. Build. Mater. 235 (2020), 117481.
[20] W. Zhang, Y. Hama, S.H. Na, Drying shrinkage and microstructure characteristics of mortar incorporating ground granulated blast furnace slag and shrinkage reducing admixture, Constr. Build. Mater. 93 (2015) 267–277.
[21] X. Zhao, C. Liu, L. Zuo, L. Wang, Q. Zhu, M. Wang, Investigation into the effect of calcium on the existence form of geopolymerized gel product of fly ash based geopolymers, Cem. Concr. Compos. 103 (2019) 279–292.
[22] N. Kabay, N. Miyan, A comparative study on the physical and mechanical properties of alkali activated materials, Sigma J. Eng. Natl. Sci. 38 (2020) 649–658.
[23] X. Dai, S. Aydın, M.Y. Yardımcı, K. Lesage, G. de Schutter, Rheology and microstructure of alkali-activated slag cements produced with silica fume activator, Cem. Concr. Compos. 125 (2022), 104303.
[24] N. Kabay, N. Miyan, H. Özkan, Basic oxygen furnace and ground granulated blast furnace slag based alkali-activated pastes: Characterization and optimization, J. Clean. Prod. 327 (2021) 129483.
[25] S. Siddique, J.G. Jang, Acid and sulfate resistance of seawater based alkali activated fly ash: A sustainable and durable approach, Constr. Build. Mater. 281 (2021), 122601.
[26] T. Yang, H. Zhu, Z. Zhang, X. Gao, C. Zhang, Q. Wu, Effect of fly ash microsphere on the rheology and microstructure of alkali-activated fly ash/slag pastes, Cem. Concr. Res. 109 (2018) 198–207.
[27] P. Shoaei, F. Ameri, H.R. Musaeei, T. Ghasemi, C.B. Cheah, Glass powder as a partial precursor in Portland cement and alkali-activated slag mortar: A comprehensive comparative study, Constr. Build. Mater. 251 (2020), 118991.
[28] R. Xiao, Y. Zhang, X. Jiang, P. Polaczyk, Y. Ma, B. Huang, Alkali-activated slag supplemented with waste glass powder: Laboratory characterization, thermodynamic modelling and sustainability analysis, J. Clean. Prod. 286 (2021), 125554.
[29] A. Saludung, T. Azeyanagi, Y. Ogawa, K. Kawai, Effect of silica fume on efflorescence formation and alkali leaching of alkali-activated slag, J. Clean. Prod. 315 (2021), 128210.
[30] J. Ren, L. Hu, Z. Dong, L. Tang, F. Xing, J. Liu, Effect of silica fume on the mechanical property and hydration characteristic of alkali-activated municipal solid waste incinerator (MSWI) fly ash, J. Clean. Prod. 295 (2021), 126317.
[31] K. Sun, X. Peng, S. Wang, L. Zeng, P. Ran, G. Ji, Effect of nano-SiO2 on the efflorescence of an alkali-activated metakaolin mortar, Constr. Build. Mater. 253 (2020), 118952.

[32] P. Perez-Cortes, K. Cabrera-Luna, J.I. Escalante-Garcia, Alkali-activated limestone/metakaolin cements exposed to high temperatures: Structural changes, Cem. Concr. Compos. 122 (2021) 104147.
[33] H. Al-musawi, F.P. Figueiredo, S.A. Bernal, M. Guadagnini, K. Pilakoutas, Performance of rapid hardening recycled clean steel fibre materials, Constr. Build. Mater. 195 (2019) 483–496.
[34] I. Ismail, S.A. Bernal, J.L. Provis, S. Hamdan, J.S.J. van Deventer, Drying-induced changes in the structure of alkali-activated pastes, J. Mater. Sci. 48 (9) (2013) 3566–3577.
[35] Y. Rifaai, A. Yahia, A. Mostafa, S. Aggoun, E.-H. Kadri, Rheology of fly ash-based geopolymer: Effect of NaOH concentration, Constr. Build. Mater. 223 (2019) 583–594.
[36] A. Fernández-Jiménez, F. Puertas, Effect of activator mix on the hydration and strength behaviour of alkali-activated slag cements, Adv. Cem. Res. 15 (3) (2003) 129–136.
[37] A. Hajimohammadi, J.L. Provis, J.S.J. van Deventer, Effect of alumina release rate on the mechanism of geopolymer gel formation, Chem. Mater. 22 (18) (2010) 5199–5208.
[38] A. Favier, J. Hot, G. Habert, N. Roussel, J.-B. d'Espinose de Lacaillerie, Flow properties of MK-based geopolymer pastes. A comparative study with standard Portland cement pastes, Soft Matter. 10 (2014) 1134–1141.
[39] D.-W. Zhang, D. Wang, Z. Liu, F. Xie, Rheology, agglomerate structure, and particle shape of fresh geopolymer pastes with different NaOH activators content, Constr. Build. Mater. 187 (2018) 674–680.
[40] F. Xie, Z. Liu, D. Zhang, J. Wang, D. Wang, J. Ni, The effect of NaOH content on rheological properties, microstructures and interfacial characteristic of alkali activated phosphorus slag fresh pastes, Constr. Build. Mater. 252 (2020), 119132.
[41] B. Chen, J. Wang, J. Zhao, R. Černý, Effect of sodium aluminate dosage as a solid alkaline activator on the properties of alkali-activated slag paste, Adv. Mater. Sci. Eng. 2021 (2021) 1–13.
[42] X. Gao, Q.L. Yu, H.J.H. Brouwers, Properties of alkali activated slag–fly ash blends with limestone addition, Cem. Concr. Compos. 59 (2015) 119–128.
[43] X. Zhu, M. Zhang, K. Yang, L. Yu, C. Yang, Setting behaviours and early-age microstructures of alkali-activated ground granulated blast furnace slag (GGBS) from different regions in China, Cem. Concr. Compos. 114 (2020), 103782.
[44] A.S.S.S. Nedunuri, S. Muhammad, Fundamental understanding of the setting behaviour of the alkali activated binders based on ground granulated blast furnace slag and fly ash, Constr. Build. Mater. 291 (2021), 123243.
[45] P.D. Silva, K. Sagoe-Crenstil, V. Sirivivatnanon, Kinetics of geopolymerization: role of Al2O3 and SiO2, Cem. Concr. Res. 37 (4) (2007) 512–518.
[46] R.H. Geraldo, L.F.R. Fernandes, G. Camarini, Water treatment sludge and rice husk ash to sustainable geopolymer production, J. Clean. Prod. 149 (2017) 146–155.
[47] E. Nimwinya, W. Arjharn, S. Horpibulsuk, T. Phoo-Ngernkham, A. Poowancum, A sustainable calcined water treatment sludge and rice husk ash geopolymer, J. Clean. Prod. 119 (2016) 128–134.
[48] A. Poowancum, E. Nimwinya, S. Horpibulsuk, Development of room temperature curing geopolymer from calcined water-treatment-sludge and rice husk ash, in: Calcined Clays for Sustainable Concrete, Springer (2015) 291–297.
[49] M. Vafaei, A. Allahverdi, Influence of calcium aluminate cement on geopolymerization of natural pozzolan, Constr. Build. Mater. 114 (2016) 290–296.
[50] S.A. Bernal, J.L. Provis, V. Rose, R. Mejía de Gutierrez, Evolution of binder structure in sodium silicate-activated slag-metakaolin blends, Cem. Concr. Compos. 33 (1) (2011) 46–54.
[51] C.-T. Chen, H.-A. Nguyen, T.-P. Chang, T.-R. Yang, T.-D. Nguyen, Performance and microstructural examination on composition of hardened paste with no-cement SFC binder, Constr. Build. Mater. 76 (2015) 264–272.
[52] C.K. Yip, G.C. Lukey, J.L. Provis, J.S.J. van Deventer, Effect of calcium silicate sources on geopolymerisation, Cem. Concr. Res. 38 (4) (2008) 554–564.
[53] G.F. Huseien, K.W. Shah, Durability and life cycle evaluation of self-compacting concrete containing fly ash as GBFS replacement with alkali activation, Constr. Build. Mater. 235 (2020), 117458.
[54] P. Nath, P.K. Sarker, Effect of GGBFS on setting, workability and early strength properties of fly ash geopolymer concrete cured in ambient condition, Constr. Build. Mater. 66 (2014) 163–171.
[55] T. Phoo-Ngernkham, V. Sata, S. Hanjitsuwan, C. Ridtirud, S. Hatanaka, P. Chindaprasirt, High calcium fly ash geopolymer mortar containing Portland cement for use as repair material, Constr. Build. Mater. 98 (2015) 482–488.
[56] D. Ravikumar, N. Neithalath, Effects of activator characteristics on the reaction product formation in slag binders activated using alkali silicate powder and NaOH, Cem. Concr. Compos. 34 (7) (2012) 809–818.
[57] M.a. Hongqiang, C. Hongyu, Z. Hongguang, S. yangyang, N.i. Yadong, H. Qingjie, H. Zetao, Study on the drying shrinkage of alkali-activated coal gangue-slag mortar and its mechanisms, Constr. Build. Mater. 225 (2019) 204–213.
[58] M. Mastali, P. Kinnunen, A. Dalvand, R.M. Firouz, M. Illikainen, Drying shrinkage in alkali-activated binders–a critical review, Constr. Build. Mater. 190 (2018) 533–550.
[59] R. Xiao, X. Jiang, M. Zhang, P. Polaczyk, B. Huang, Analytical investigation of phase assemblages of alkali-activated materials in CaO-SiO2-Al2O3 systems: The management of reaction products and designing of precursors, Mater. Des. 194 (2020), 108975.